SURFACE SOIL MOISTURE RETRIEVAL USING REFLECTOMETRY OF S-BAND SIGNALS OF OPPORTUNITIES

A Thesis

Submitted to the Faculty

of

Purdue University

by

Archana Suhas Choudhari

In Partial Fulfillment of the

Requirements for the Degree

of

Masters of Science in Aeronautics and Astronautics

August 2020

Purdue University

West Lafayette, Indiana

THE PURDUE UNIVERSITY GRADUATE SCHOOL
STATEMENT OF THESIS APPROVAL

Dr. James L. Garrison, Chair

School of Aeronautics and Astronautics

Dr. Arthur E. Frazho

School of Aeronautics and Astronautics

Dr. Dara Entekhabi

Neil Armstrong Distinguished Visiting Fellow

Approved by:

Dr. Gregory A. Blaisdell

Head of the School Graduate Program

To my parents, Dr. Suhas Y. Choudhari and Dr. Balapraveena S. Choudhari

ACKNOWLEDGMENTS

First and foremost, I would like to thank my research guide and advisor, Dr. James Garrison, for giving me the opportunity to work on this project and providing invaluable guidance throughout this journey.

Besides my advisor, I would like to thank my committee members Dr. Arthur Frazho and Dr. Dara Entekhabi, for the opportunity.

I want to offer my gratitude to my fellow labmates at the Radio Navigation Lab for the stimulating discussions, for their guidance and help during the time of need, and all the fun times. Special thanks to Benjamin Nold for his meticulous data collection from the tower experiment in 2017 and 2018, without which my research would not have taken place.

My heartfelt thanks to Dylan Boyd and Prof. Kurum from Mississippi State University for the SCoBi model results. Thank you for all the prompt replies and in-depth discussions on the SCoBi model.

I am extremely grateful to my family- my parents, Dr. Suhas Choudhari and Dr. Balapraveena Choudhari, for the motivation, for the moral and financial support and their prayers. My brother, Anirudh Choudhari, for all the laughter during the hard times. I want to thank my best friends- Sruthi Chengalrayan and Utsav Niroula, for the moral support and keeping me mostly sane. They all kept me going.

TABLE OF CONTENTS

Page

LIST OF TABLES

LIST OF FIGURES

Figure Page

SYMBOLS

λ	Wavelength
s	Root Mean Square surface height
θ_i	Incidence angle
θ	Elevation angle
θ_r	Reflection angle
x_D	Direct signal
x_R	Reflected signal
Γ	Reflectivity
τ	Lag
B	Bandwidth of the channel

ABBREVIATIONS

ESA	European Space Agency
NASA	National Aeronautics and Space Administration
SMOS	Soil Moisture Ocean Salinity
SMAP	Soil Moisture Active Passive
GNSS	Global Navigation Satellite Systems
GPS	Global Positioning System
GNSS-R	Global Navigation Satellite System- Reflectometry
SoOp	Signals of Opportunity
ACRE	Agronomy Center for Research and Education
XM	XM Satellite Radio
SCoBi	SoOp Coherent Bistatic
SNR	Signal-to-Noise Ratio
SDARS	Satellite Digital Audio Radio Services
FCC	Federal Communications Commissions
TDR	Time Domain Reflectometry
SSM/I	Special Sensor Microwave Imager
SoOp-AD	Signals of Opportunity Airborne Demonstrator
RFI	Radio Frequency Interference
PRN	Pseudorandom Noise
MEO	Middle Earth Orbits
CYGNSS	CYclone Global Navigation Satellite Systems
TDS-1	Technology Demonstration Satellite-1
DDM	Delay-Doppler Maps
rSNR	Relative Signal-to-Noise Ratio
NCAR	National Center for Atmospheric Research

QPSK	Quadrature Phase-Shift keying
TDM	Time Division Multiplex
PSD	Power Spectrum Density
EIRP	Effective Isotropically Radiated Power
C/N0	Carrier to Noise Power
RF	Radio frequency
LHCP	Left Hand Circularly Polarized
RHCP	Right Hand Circularly Polarized
USRP	Universal Software Radio Peripheral
RMS	Root Mean Square
RTD	Resistance Temperature Detector
FFT	Fast Fourier Transform
IFFT	Inverse Fast Fourier Transform
SAF	Self-Ambiguity Function
SMC	Soil Moisture Content

ABSTRACT

Choudhari, Archana S. MS, Purdue University, August 2020. Surface Soil Moisture Retrieval using Reflectometry of S-band Signals of Opportunities. Major Professor: James L. Garrison.

Surface soil moisture is one of the few direct hydrological variables which can be measured. It plays a crucial part in the water cycle, agriculture, drought development, runoff generation, and many other phenomena. Satellite observations from active and passive microwave radiometers are best suited for the retrieval of soil moisture. The relationship between soil dielectric constant and water content is direct and is used to determine the surface soil moisture levels. Active microwave remote sensing techniques measure the energy reflected from target surfaces (ocean, soil, biomass) after transmitting a pulse of microwave energy, whereas passive microwave sensors measure the self-emissions of the target surfaces. The passive missions by ESA's SMOS and NASA's SMAP have demonstrated this technology for remote sensing on a global scale. Global Navigation Satellite System-Reflectometry (GNSS-R) is an alternative approach to the remote sensing of soil moisture, as demonstrated through several airborne and ground-based experiments. The new technique of Signals of Opportunity (SoOp) uses a bistatic radar configuration in which the non-cooperative transmitter already transmits signals designed for communication or navigation. The receiver reuses the reflected energy from the target surface (ocean, soil, biomass), thereby making the digital communication and navigation signal spectrum useful to the remote sensing science community. Several airborne and ground-based experiments have been conducted on the use of digital communication signals, a range of frequencies from P-band to Ku-band, for measurement of ocean surface roughness, wind speed, and soil moisture.

This thesis presents the preliminary results obtained for reflectivity retrievals for the 2017 and 2018 S-band tower-based SoOp field experiment conducted at Purdue's Agronomy Center for Research and Education (ACRE). XM signals were recorded by a sky-facing antenna and an Earth-facing antenna mounted atop a tower. The line-of-sight (direct) signal is captured by the sky-facing antenna and reflected signal from the soil captured by the Earth-facing antenna was used for the ambiguity function of XM transmission. A link budget was used to determine the received signal to noise ratio (SNR). The cross-correlation between the direct and the reflected XM signals was used to estimate reflectivity values. The reflectivity retrievals were compared with the in-situ soil moisture content at 5 cm depth obtained by the HydraProbes. The reflectivity values were also verified by a Signals of Opportunity (SoOp) Coherent Bistatic (SCoBi) simulated model.

1. INTRODUCTION

Soils are composed of solids, liquids, and gases mixed in variable proportions. Soil texture depends on the size of the particles, and the structure of soil depends on the arrangement of soil particles [1]. Colour, texture, and density of soil comprise the physical properties, whereas the electrical properties include dielectric constant, conductivity, and permeability. The dielectric properties and the water content of soil are dependent on each other. As soil moisture increases, the free water content increases, and this free water changes the dielectric constant. There is a significant difference in the dielectric properties of dry soil, wet soil, and water, which is utilized for determining the volumetric soil moisture content using microwaves, remotely. Reflectivity from the soil determines the water content. Therefore, the microwave spectrum is used to estimate the soil moisture by determining the reflectivity.

The estimation of soil moisture content in the topsoil (0 - 5 cm) and the root-zone (5 cm - 1 m) is of importance. Soil Moisture is a direct hydrological variable that impacts the global environment. The weather cycle, water cycle, agriculture, the evaporation process in the topsoil, vegetation transpiration, surface runoff, and drought development are few processes that can be estimated with the knowledge of soil moisture [2]. Due to its significance, soil moisture has been included in the list of the most fundamental climate variables by the Global Climate Observing System initiative that is co-sponsored by the World Meteorological Organization [3]. The different processes involved in the water cycle are shown in Fig. 1.1.

Numerous studies have shown the importance of land-surface feedback with the global climate changes [5] [6]. The main variables in the land-surface hydrology include soil moisture, surface temperature, vegetation, and streamflow [7]. Most of these variables can be observed with satellites and in-situ measurements. Soil moisture remains the only variable with its spatial and temporal variations across scales, which

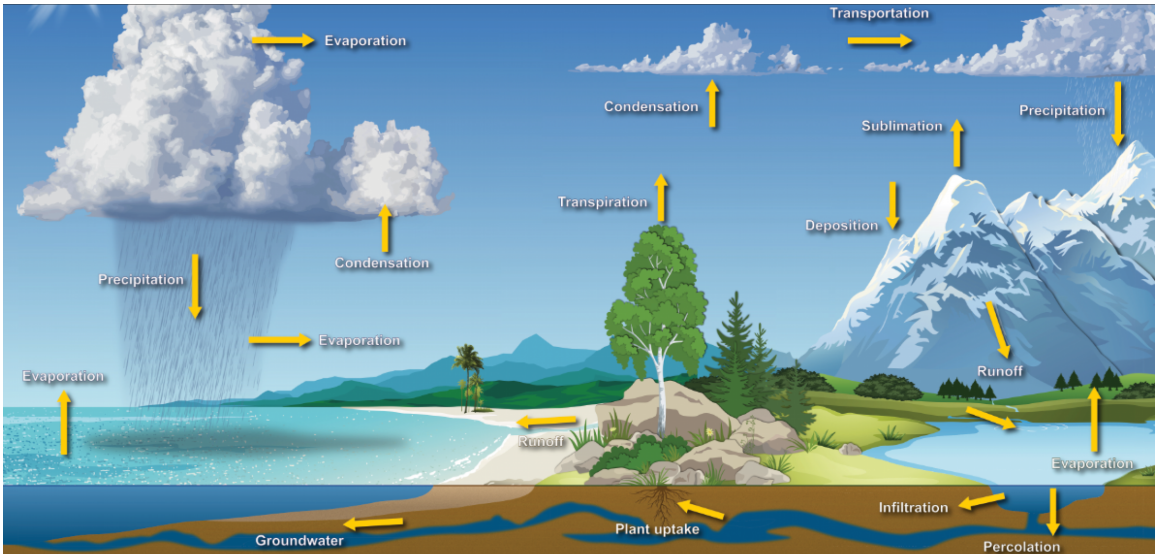

Figure 1.1. The Water Cycle [4]

makes it difficult to estimate only with in-situ measurements. Due to this reason, it is necessary to understand the relationship of soil moisture to these phenomena on small and large spatial scales and over time. Temporally, the soil moisture measurements need to be taken in order of minutes (before and after a precipitation event), in order of hours (for surface runoff), and order of days or months (for freeze-thaw conditions and overall climate conditions) to understand the environmental processes.

1.1 Soil Moisture Measurement Techniques

The study of soil moisture measurements has been going on for centuries. The first methods used for soil moisture measurements were developed for field conditions only. Various types of equipment and techniques were designed for the measurement of soil moisture. The methods included as primitive as feeling the soil for moisture content, to complicated electronic equipment using radioactive substances [8].

With the recent technological advances, the usage of satellites, aircraft, drones, and efficient electronic instruments, is the emerging technique for measuring soil mois-

ture content. At the pedon scale, electromagnetic soil moisture sensors based on the time-domain reflectometry (TDR), impedance, or capacitance measurement principles are used for soil moisture records. The state-of-the-art technology incorporates microprocessors to communicate data to a data logger connected with wireless networks to record the data with high temporal frequency [3]. At a large spatial scale, a Special Sensor Microwave Imager (SSM/I) was used in the 1980s to record soil moisture values on a continental scale [9].

1.1.1 Gravimetric soil measurements

The gravimetric method involves the collection of a soil sample from the site, weighing the sample, drying it in an oven to evaporate the water, and weighing the same sample again [10]. The loss in the weight of the soil sample is calculated as the soil moisture content. This method is the oldest method utilized for soil moisture measurements used in the late '80s and early '90s [8]. Gravimetric soil measurements these days are precise, but temporally and spatially limited. There are many other disadvantages to this method. The soil sample must not contain any organic mass such as grass, twigs, etc. which can alter the weight of the soil after drying. It is an arduous process of collection for such a soil sample, sometimes a few feet from the top surface of the soil. The field has to be visited multiple times to obtain a soil sample in case of a rain event. If multiple samples were taken, each sample needs to be identified, per the location and the time of collection and stored properly.

With the advancement in technology, the electronic instruments and sensors used in the gravimetric analysis of soil have improved drastically. They are based on the time-domain reflectometry (TDR), impedance, or capacitance measurement principles. The sensors are connected with wireless networks to provide for temporal soil moisture changes. This resolves the factor of temporal resolution, but spatial diversity is still not achieved as the measurements are "point-based." The HydraProbes used in the in-situ soil moisture values for the tower-based experiment in 2018 is an

example of a state-of-the-art gravimetric soil measurement instrument, shown in Fig. 1.2.

Figure 1.2. The HydraProbes used for in-situ measurements for tower experiment 2018 [10]

1.1.2 Active and Passive Radiometry

The microwave portion of the electromagnetic spectrum ranges from 1 mm to 1 m in wavelength. Due to the longer wavelengths, as compared to the visible or infrared spectrum, microwaves are ideal for remote sensing as they can penetrate through clouds, biomass, rainfall, dust, and smoke. This property of microwave frequencies allows for data collection during mostly all types of weather conditions [11]. The penetration depth of the microwaves depends on the wavelengths. P-band (wavelength: 1.2 m - 60 cm) can penetrate the root-zone (up to 1 m beneath the surface), L-band (wavelength: 60 - 20 cm) can penetrate the atmosphere, snow, and light vegetation to the top 10 cm of the soil, and S-band (wavelength: 15 cm - 7.5 cm) can penetrate up to 5 cm of the topsoil [10]. The penetration depth also varies with the density and type of soil [12].

Active remote sensing

Active radar provides for the illumination of the target, and the same instrument records the backscattered signals. The emissive and scattering characteristics of soil depend on soil moisture, amongst other variables. The backscattered emissions from the soil are modified by soil moisture, modulated by surface roughness, above-ground biomass effects, and interaction with the atmosphere before being received by a sensor. The backscattered radiations are used to determine the topography, soil moisture content, surface, and ocean wind speeds.

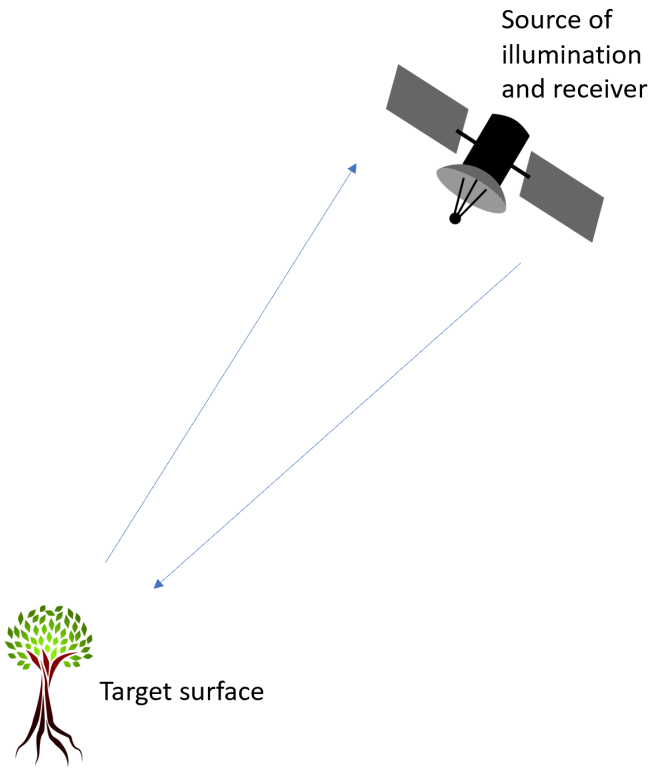

Figure 1.3. Active Remote Sensing

Passive remote sensing

All objects emit microwave radiations, albeit very small amounts. The passive microwave sensors detect emitted radiations from the surface. These measurements are made only in the protected bands and the lowest protected band is 1.4 GHz.

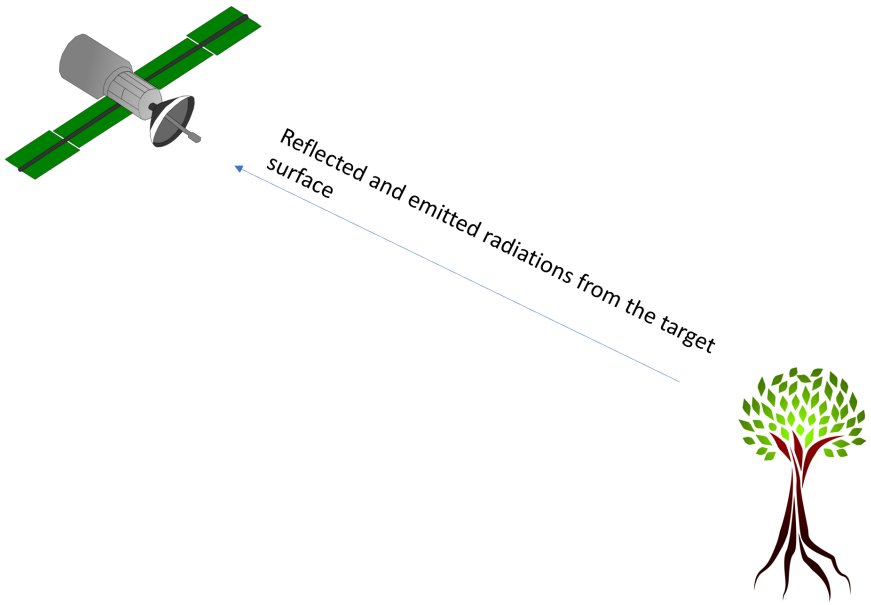

Figure 1.4. Passive Remote Sensing

Space-borne remote sensing

NASA Soil Moisture Active Passive (SMAP) mission [13] and ESA Soil Moisture and Ocean Salinity (SMOS) [14] were the first of the Earth observation satellites dedicated for remote sensing of soil moisture. SMAP incorporated an L-band radar and L-band radiometer for estimation of soil moisture with 10-30 km resolution and sensing depths limited up to 10 cm.

SMAP operates as a passive radiometer in the microwave frequencies of L-band (1.41 GHz) and used to operate functionally as an active radar operating at 1.26 GHz

before ceasing operation on July 7, 2015. The "synthetic aperture" technique allowed SMAP to spatially resolve a 9 km area for soil moisture measurements and a 3 km area for the freeze-thaw state. SMAP maps the equatorial region every three days and the polar region every two days. The passive radiometer, completely functional, accurately measures the emitted RF radiations. This receiving frequency is only allocated for the receiver, by the Federal Communications Commissions (FCC), to operate without any interference. SMAP measures the "microwave temperatures" of the target surface. The water appears "colder" (about 100 K) as compared to dry soil (about 300 K). This wide difference in the temperatures allows for accurate soil moisture measurements [15].

1.1.3 Bistatic remote sensing using Signals of Opportunities (SoOp)

Bistatic remote sensing is a technique involving a radar system where the transmitter and receiver are separate. SoOp receivers reuse the signals transmitted from a different, already established, active source (such as satellites for navigation and communication signals). Frequencies for SoOp are not limited, unlike the active systems restricted due to spectrum allocations and competition for protected bands for science communities. This technique expands the spectrum to communication and navigation bands for remote sensing and earth sciences [16] [17] [18].

SoOp was first utilized for ocean winds applications using Global Navigation Satellite Systems (GNSS) as a source of illumination [19]. Studies demonstrate that any digital communication signal can be used as a source of illuminating for SoOp [20].The graphical representation of the SoOp bistatic radar configuration is shown in Fig. 1.5.

In addition to the research on GNSS-Reflectometry (GNSS-R) for Earth remote sensing, using other signals of opportunity for bistatic radar such as Broadcast signals allocated for space-to-earth communications, ranging from P- to Ka-band, are under study for multiple Earth science applications [21] [18]. The results from the first airborne campaign for soil moisture remote sensing using reflectometry of P-band

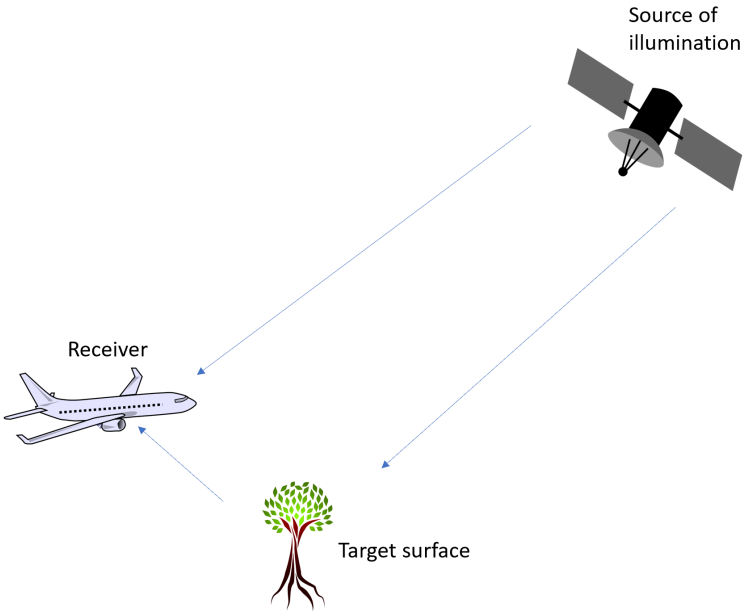

Figure 1.5. Representation of Bistatic Remote Sensing Configuration

Signals of Opportunity Airborne Demonstrator (SoOp-AD) confirm the trend of high reflectivity values over water as compared to the reflectivity values over land [18].

1.2 Outline

This thesis focuses on the S-band signals from SiriusXM Satellite Digital Audio Radio Services (SDARS), a US-based nation-wide consumer radio, operating in the frequencies 2.32 - 2.345 GHz, as the active transmitter. A specially designed instrument was mounted on a 32 m tall mobile antenna tower as the receiver. The data campaigns were conducted at Purdue's Agronomy Research Center and Education (ACRE) agricultural land, measuring bare soil and corn growth cycles in 2017 and 2018. The outline for the main body of the thesis is as follows: Chapter 2 provides the background on the history of GNSS-R used for soil moisture retrievals, an overview of the XM signals and its usage as a SoOp, and the description of the field experiment conducted in 2017 and 2018 at ACRE. Chapter 3 presents the theory of the geome-

try, the assumptions in the post-processing of the data, and the theoretical derivation of the reflectivity equation. Chapter 4 provides an overview of the data processing algorithms, and identified cases of Radio frequency interference (RFI) observed in post-processing of the data. Chapter 5 presents the preliminary results of reflectivity retrievals and their comparisons with in-situ data collected by HydraProbes and SCoBi model for the 2017 experiment. Chapter 6 summarizes the thesis and provides for several conclusions, as well as offers suggestions for future work.

2. BACKGROUND

Bistatic reflectometry has emerged as the new technique for remote sensing. Signals of Opportunity in a Bistatic configuration, using Global Navigation Satellite System (GNSS) signals reflected from the sea surface, was used to measure sea surface roughness, ocean winds, soil moisture, and ice [22] [23] [24] [25]. Since 1993, the source of illumination in these bistatic radar systems are the Global Navigation Satellite System (GNSS) signals [22]. These studies examined the shape of the waveform formed by cross-correlating the reflected GNSS-Reflectometry (GNSS-R) signals with a copy of the Pseudorandom Noise (PRN) code over a range of delays. The cross-correlated waveforms were observed to be sensitive to the ocean surface roughness and ocean winds [16].

2.1 GNSS-R for Earth Remote Sensing

The usage of GNSS signals as the source of illumination in a bistatic configuration is well established [22] [23] [24]. GNSS-R measurements from satellites provide global coverage as GNSS is a constellation of satellites. The United States' Global Positioning System (GPS), globally available since 1994 [26], is one of the global navigation satellite systems (GNSS) consisting of 32 satellites in the Middle Earth Orbits (MEO). It operates on L-band (1.57542 GHz (L1 signal) and 1.2276 GHz (L2 signal)). The GPS signals are continuously broadcast encoded with PRN codes: C/A code, for civilian use, whereas the P-code, for U.S. military use.

The shape of the correlation function of the GPS reflected signals with the local copy of the incoming GPS signal was observed to be dependent on the sea surface roughness and ocean winds [24]. An investigative study demonstrating soil moisture remote sensing with observations from the UK TechDemoSat-1 satellite mission (TDS-

1) was conducted in 2016, which used Delay Doppler Maps (DDM) to estimate ocean wind directions and speeds [27]. The DDM measures both the delay that a reflected signal takes to get back to the receiver and the doppler (frequency) shift of that signal. This technology has also been demonstrated in space with the launch of the CYclone GNSS (CYGNSS) ocean winds sensing constellation in 2016 [28]. The CYGNSS mission uses eight micro-satellites to measure wind speeds over Earth's oceans, with the purpose of understanding and predicting cyclones. It was noted that a soil moisture product could be derived from the CYGNSS data under limited conditions. An investigative study performed by [29] introduced a relative signal-to-noise ratio (rSNR) value from a CYGNSS-derived delay-Doppler map to improve the temporal resolution of soil moisture derived from SMAP data. However, GPS signals used by CYGNSS are also in L-band, and thus, the observed depth of soil moisture would not be an improvement over that provided by L-band radiometry. The results from [29] proved that synergistic use of CYGNSS observations could improve soil moisture estimates from current satellite systems like SMAP and SMOS.

Another investigation conducted using GPS land-reflected signals in 2002 found to follow the general soil moisture trend as a function of time (SMEX02). The GPS receiver was mounted on the NCAR C-130 aircraft to make co-located measurements with other instruments. The initial results from the first controlled experiment of GPS bistatic radar for soil moisture remote sensing suggested that the technique is sensitive to temporal and spatial variations in soil moisture [19].

In addition to the research on GNSS-R for Earth remote sensing, studies have also been done on using other signals for bistatic radar configuration. Most notably, significant work has been conducted on the use of communication satellite transmitters as signals of opportunity [30] [31]. It was demonstrated in 2012 that any digital communication signals could be used as a source of illumination for SoOp [17]. An important finding was that along with higher SNR, communication signals are also encrypted. Therefore, cross-correlation can be performed between the direct and reflected signals, without the need for a model signal or a local copy of the direct signal.

A flight campaign was conducted in Little Washita, Oklahoma, in October 2016 using P-band SoOp. The coverage included land and Lake Ellsworth as a calibration source. The reflectivity values over the lake were evidently higher than over land surfaces [18]. S-band signals have also been used as a source of illumination for bistatic radar remote sensing for estimation of surface wind speeds [16].

2.2 XM Radio Signals

The XM signal occupies a spectrum allocation between 2332.5 MHz to 2345.0 MHz (S-band). XM is the most popular Satellite Digital Audio Radio Service (SDARS) in the United States and Canada operated by Sirius XM Radio Inc. XM provides digital programming directly from two high-powered satellites in geostationary orbit above the equator: XM Rhythm at 85°west longitude (XM-3) and XM Blues at 115°west longitude (XM-4) along with a network of ground-based repeaters. The spectrum allocation is divided evenly between two separate, but co-owned, SDARS networks, Sirius and XM. The spectrum allocation of Sirius and XM frequencies, by Federal Communications Commissions (FCC) is depicted in Fig 2.1.

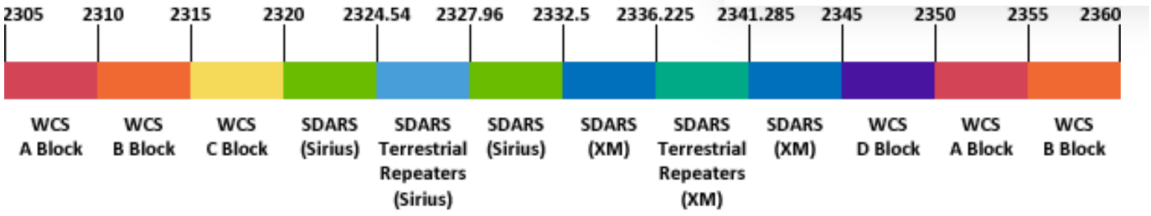

Figure 2.1. SDARS Spectrum allocation by FCC [32]

Terrestrial repeaters for XM satellite radio are at Indianapolis, Fort Wayne, and Kokomo [33] near ACRE, the interested field of study. Since there are no repeaters in the West Lafayette area, the repeater bands show up mostly as noise bands in the

observed spectrum. Some cases of unusually high RFI is noted in the noise bands during certain times of the day mentioned in Chapter 4.

2.2.1 XM frequency and signal structure

The XM signal occupies a spectrum allocation between 2332.5 MHz to 2345.0 MHz (S-band), as seen in Fig 2.1. Each satellite, XM-3, and XM-4 transmits two carriers (to make it a total of four carriers for the system). The two carriers contain half the power of the XM system. For simplified radio antenna, all satellite downlink signals have the same Left Hand Circular Polarization (LHCP) [34]. The bandwidth of each channel is 1.886 MHz. Each channel is distinguished by the dip and contains a single Quadrature phase-shift keying (QPSK) modulated Time Division Multiplexed (TDM) signal with a symbol period of 3.28 Mbps.

Each satellite uses a different coding scheme for robust signals. In this thesis, a specially designed instrument, using P-band and S-band signals, was used for data campaigns in 2017 and 2018 at ACRE. The data was collected for bare soil and various corn growth cycles. The timeline of the experiment is presented in Appendix A. In this thesis, the data processing of S-band for reflectivity retrievals is performed only over bare soil. The Power Spectrum Density (PSD) of the direct XM-3 and XM-4 signals, with a sampling frequency of 8 MHz, after post-processing the signals recorded in the field experiment in 2017, is presented in Fig. 2.2. It is noted that the distinctive dip in the spectrum denotes the separation between the XM-3 and XM-4 frequencies.

The link budget used for XM signals in the 2017 and 2018 Purdue SoOp Tower experiment is shown in Table 2.1. The link budget analysis for the XM signals is performed to estimate the SNR.

The brightness temperature is different for the sky-view and earth-view antennas. Microwave systems have wideband noise from multiple sources, include thermal background noise. Following convention, the ground brightness temperature was chosen

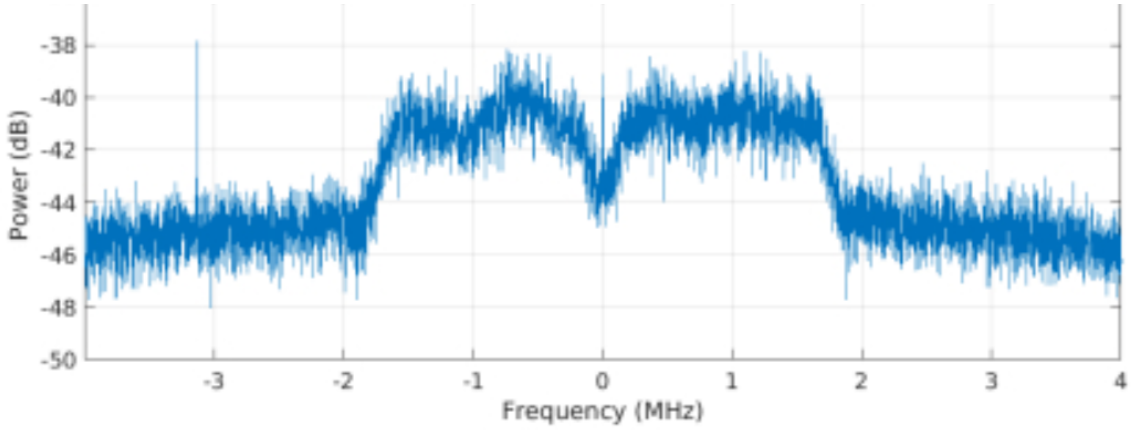

Figure 2.2. Spectrum of XM satellite signal recorded by the USRP in the through state for the field experiment 2017

Table 2.1. Link Budget for Purdue SoOp Tower Experiment [10]

	S Band 2017	**S Band 2018**	**Units**
Signal Name	XM Radio	XM Radio	
Bandwidth	1.64	1.64	MHz
EIRP	68	68	dBW
Range	37,535	37,535	km
Free Space Loss	191.34	191.34	dB
Atmospheric loss	0.5	0.5	dB - Arbitrary
Polarization Loss	0	0	dB
Antenna Gain	3	3	dBi
Power at Frontend	-125.83	-125.83	dBW
Noise temperature system	329.38	62.67	K
C/N0	20.14	27.731	dB

to be 290 K, the horizon was chosen to be 75 K, and the sky was selected to be 2.7 K [10].

2.3 Purdue SoOp Tower Experiment 2017 and 2018 [10]

The tower-based SoOp instrument used frequencies in the P-Band and S-Band for the data campaigns in the summers of 2017 and 2018 at Purdue's ACRE in field #23. The soil type in #23 was loam type. The soil texture and type must be known for accurate soil moisture measurements. The instrument was designed to set atop a 32 m tall mobile antenna tower. The antennas and the corresponding Radio-frequency (RF) front end instrument were also mounted on the tower. The digital receiver was placed on the ground, and RF signals (coax) cables were used to connect them. All the electrical cables used in the experiment were double shielded to reduce RFI. The location of the trailer and the sensors in the 2017 and 2018 had minor variations. The cornfield had drainage tiles installed 1 m below the surface to assist in water drainage. The tiles ran east to west and spaced 20 m apart north to south. The difference in location of the tower and the in-situ sensors for the 2017 and 2018 experiments from Google Earth Imagery are shown in Figure 2.3.

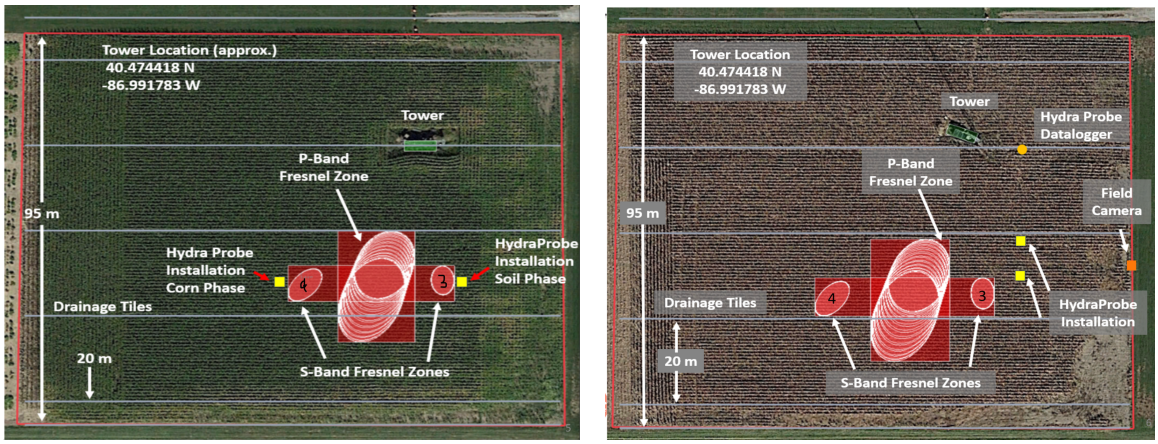

Figure 2.3. Difference in the location of instrument for SoOp Tower experiment [10]

The system-level block diagram of the instrument is shown in Fig. 2.4.

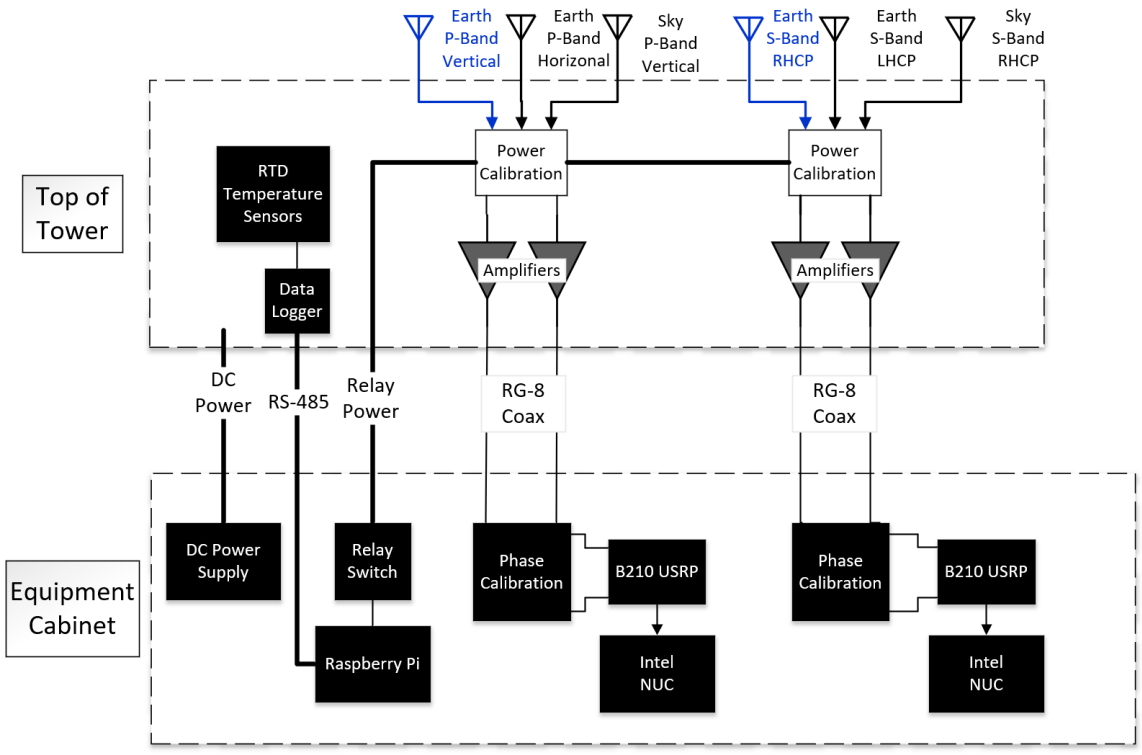

Figure 2.4. System block diagram of instrument for SoOp tower experiment [10]

2.3.1 S-band antenna and system configuration

The configuration of the microwave front end system was nearly the same for 2017 and 2018, except for the single-polarization earth-view antenna used for S-band in 2017, which was Left Hand Circularly Polarized (LHCP). For 2018, a Right Hand Circularly Polarized (RHCP) earth-view antenna was added to the system as depicted by the blue antenna in Fig. 2.4. Satcom 2M23P-XS-2 antennas were used for the sky-view (RHCP signal) and earth-reflected signals, respectively. This signal was then recorded using a Universal Software Radio Peripheral (USRP). In 2017, the S-Band antennas were mounted on 2 ft x 4 ft wide aluminum plates reused from an earlier experiment. The antenna gain pattern for S-band antennas was hemispherical.Published values for S-Band antenna brightness temperature values were used.

Figure 2.5 shows the P-Band and S-Band antennas mounted on the trailer. In 2018 the S-Band antennas were placed on two smaller aluminum plates as shown in Fig. 2.6.

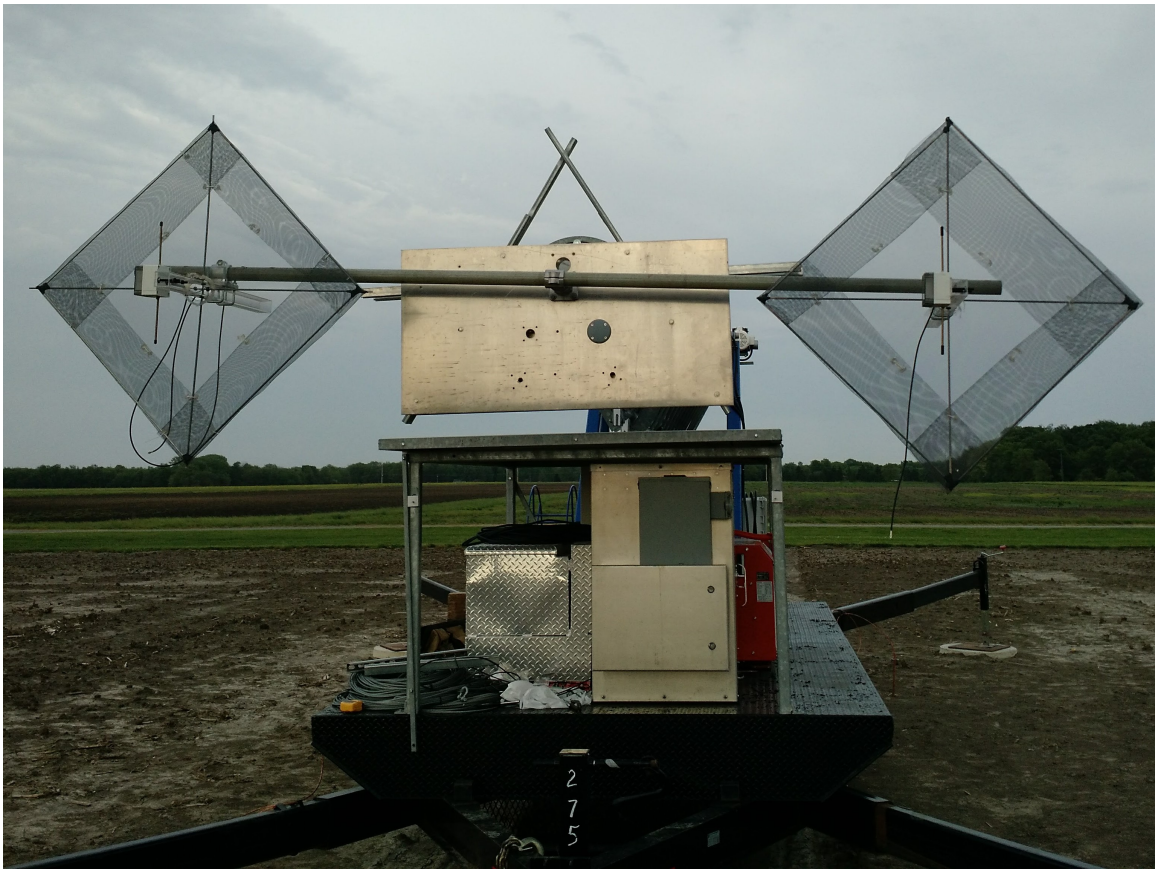

Figure 2.5. Antennas used for 2017 experiment for S- and P-bands [10]

2.3.2 RF Front end design

The RF front end was installed on top of the tower in an aluminum wash-down enclosure for reduced RFI and protection from weather elements. For the 2017 experiment, the front end could only record single earth antenna polarization (LHCP) for S-Band. In 2018, two earth-view antennas, both LHCP and RHCP, were used to

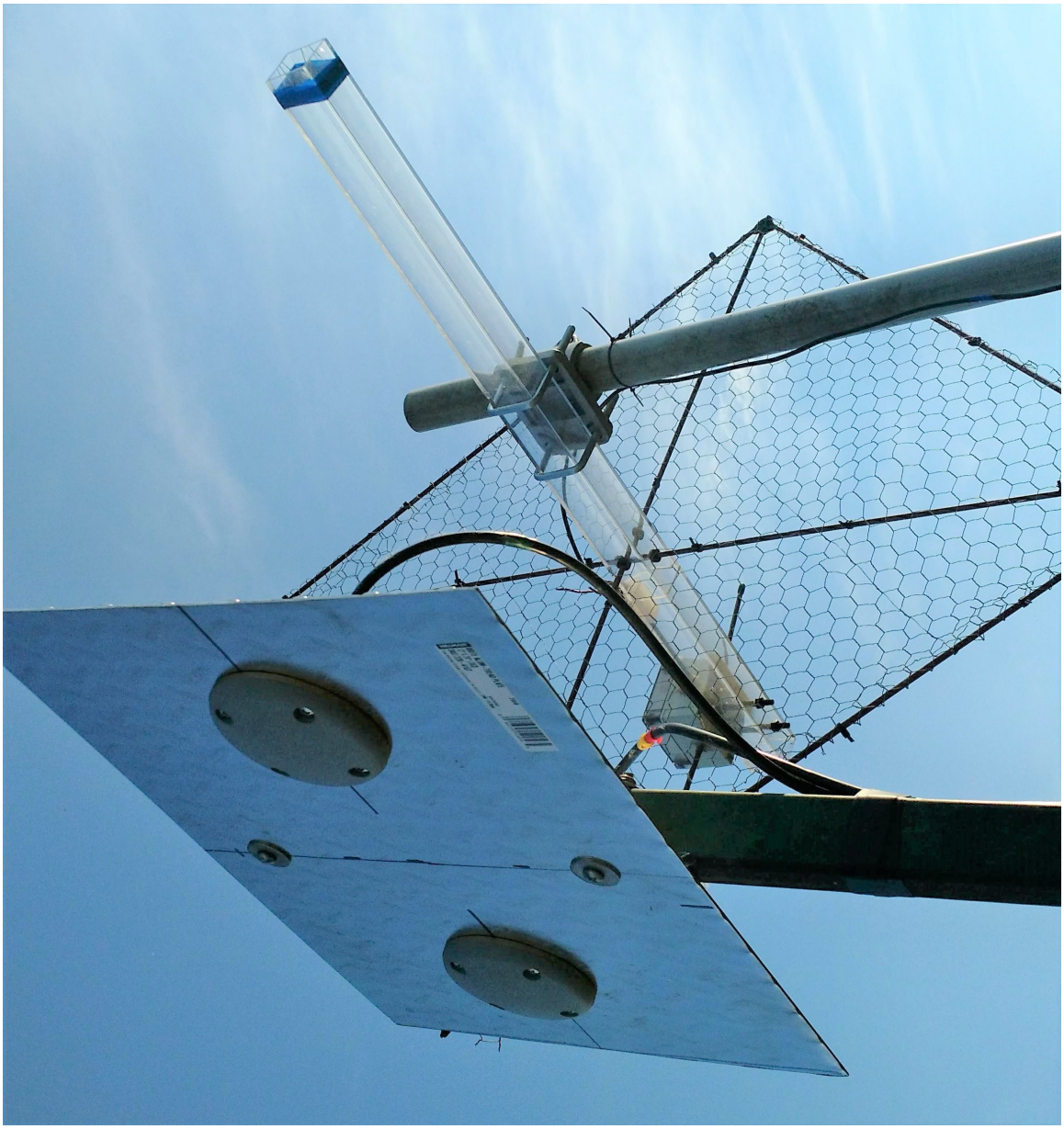

Figure 2.6. LHCP and RHCP antennas used for 2018 experiment for S-band [10]

record reflected S-band signals. The digital receiver input was time-multiplexed using a reflective RF switch. A transfer switch was used to perform antenna swapping between the direct and reflected front end paths for calibration states. The Microwave block diagram of S-band is shown in Fig 2.7.

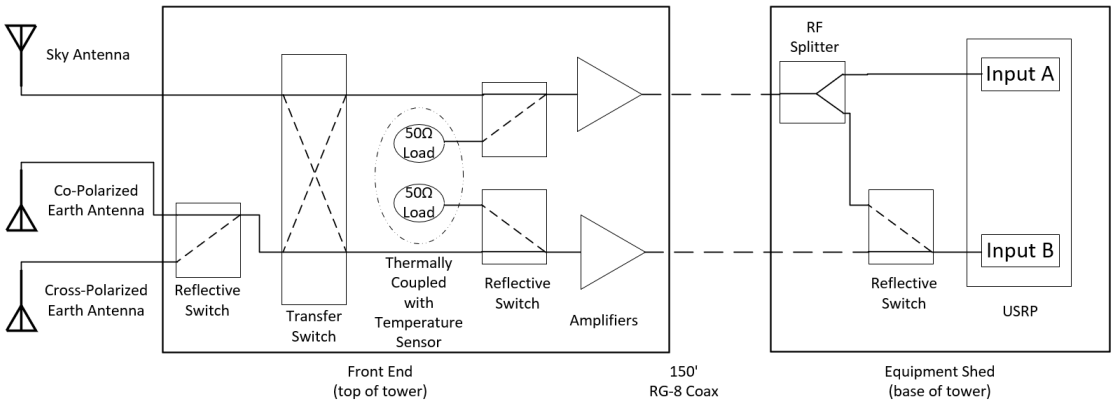

Figure 2.7. S-band block diagram [10]

2.3.3 Calibration States

The front end contained reflective and transfer switches to swap in a load, switch antennas to alternate reflected polarization, and to exchange the antennas between the sky-view and earth-view amplifier/filter chains. The different calibration states for 2017 and 2018 followed a specified time sequence, encoded to aid in post-processing state retrieval. The states were asynchronous to the RF recording. The four calibration states were: Through, Swap, Phase, and Load states. Table 2.2 provides the time-duration for each calibration state. For the 2017 experiment, the phase state was not activated. Instead, the load state was repeated for 2 seconds instead of phase state. This cycle was repeated every 20 seconds.

The through state represents the data recorded from the respective antenna channels, i.e., sky-antennas observing the direct signals at Input A of the USRP and the earth-antennas observing the reflected signals at Input B of the USRP. In the swap state, the transfer switch was used to swap the antennas between sky and earth channels, i.e., Input A received reflected signals, and Input B received direct signals. Reflective switches were used to switch in matched loads into the receiver chains. In the load state, both the inputs A and B of the USRP received matched loads having

Table 2.2. Calibration States for 2017 and 2018 S-band

Calibration state	**S Band 2017 (in sec)**	**S Band 2018 (in sec)**
Phase state	N/A	1
Through state	9	9
Load state	1 and 2	2
Swap State	8	8

the same noise temperature as the loads were connected via a copper wire. This was done to create a heat sink and tie the temperatures. A temperature sensor was placed on the copper wire. A reflective switch was used to connect the sky antenna and amplifier chain into both inputs. This was added to verify that the phase of the two input channels of the digital receiver was synchronized.

2.3.4 Data recording and management

An Ettus Universal Software Defined Radio B210 unit was used for digitizing the RF signals. The B210 has two phase coherent recording channels, thereby enabling a single unit for recording both the direct and the reflected signals. Each B210 was connected to a desktop computer via USB 3.0. The computers ran custom recording software for the USRP. 8 TB external hard drives were used to store the data temporarily and for physical transportation between the experiment site and Purdue university for long term storage and processing. The experiment generated approximately 11.13 TB a week of raw sample data. The recording computers copied the data onto external USB hard drives. The hard drives were retrieved weekly and copied onto Purdue's tape database archive system. The hard drives were stored for redundancy.

2.3.5 In-situ sensor locations

The HydraProbes were the in-situ soil moisture measurement devices inserted at depths of 5 cm, 10 cm, 20 cm, and 40 cm below the surface of the soil. The location of the HydraProbes for the 2018 experiment is shown in Fig. 1.2. HydraProbes measure soil dielectric permittivity, salinity, and temperature by transmitting a 50 Mhz radio frequency signal [35]. A Campbell Scientific CR300 data logger was used to interface with the HydraProbes. The readings were taken every 15 minutes of the four HydraProbe analog voltages and the complex dielectric measurements. The dielectric values were converted to volumetric soil moisture content due to the direct relationship between the two variables. The probes were not placed vertically below one another to avoid blocking the natural flow of water. For the 2017 experiment, the HydraProbes were placed mid-way between the northern and the southern drainage tiles. It was noted that due to a precipitation event, the field would drain rather quickly over the drainage tile as compared to the rest of the area. Therefore, another set of HydraProbes were added on the northern tile for the 2018 experiment.

Handheld theta probes were also used to measure the surface soil moisture at each sampling location. Each probe was 10.16 cm (4 inches) long and was vertically inserted at three locations: cornrow, 1/4 between two cornrows, and halfway between the cornrows, as shown in Fig. 2.8.

2.3.6 Gravimetric soil sampling and corn growth measurements

Gravimetric soil samples were collected every week from depths of 5cm, 10 cm, 20 cm, and 40 cm below the soil surface. The samples were placed in sample tins of dimensions 5 cm x 5 cm x 5 cm and were transported from the experiment site to the National Soil and Erosion lab on Purdue's campus, where they were weighed and dried and weighed for soil moisture content.

This thesis does not provide results for the corn growth cycle. However, the data was collected during the bare soil phase, corn plantation, and corn growth phase.

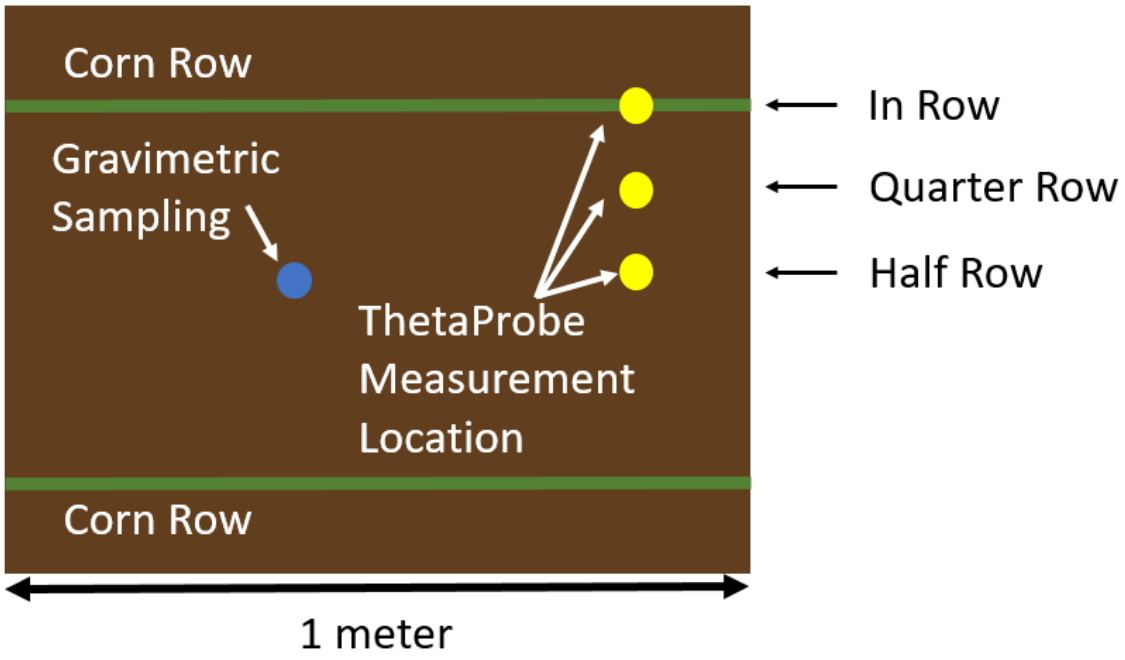

Figure 2.8. Location of theta probes [10]

The corn growth measurements were performed weekly, as well. Three plants were picked within one meter that represented the average for the sampling area. The number of corn plants per m^2, row spacing, plant height, stalk diameter, number of leaves, number of cobs, leaf height, and length from the bottom, middle and top leaf were measured. The measurements were made in the field. Then the plants were removed and taken back to Purdue's Indiana Corn and Soybean Innovation Center, where the plant was separated into the stalk, leaves, and cobs. For each sampling site, the three plants were placed in brown paper bags, weighed, dried in Wisconsin ovens then weighed again to determine water weight [10].

3. THEORY

The geometry involved in the tower-based experiment, the assumptions in the post-processing of the data, and the theoretical derivation of the reflectivity equation based on the calibration states used in this experiment are presented in this chapter.

3.1 Reflection Geometry

The tower-based S-band SoOp for reflectivity retrievals used a bistatic radar configuration. The XM-3 and XM-4 satellites were used as the active transmitters, and the instrument designed by [10] was mounted on top of a mobile antenna tower as the receiver. The instrument had a sky-view antenna to capture direct signals and an earth-view antenna to observe reflected signals from the soil. The antennas were mounted at the height of 32 m (tower height) above the reflection point on the ground.

3.1.1 Assumptions

A single ray path model was used in this configuration of bistatic SoOp tower-based experiment. Fig. 3.1 depicts the basic geometry of the problem. The assumptions made for this experiment are as follows:

1. The distance between the transmitter and receiver antennas is infinity.
    - Since the transmitter is a satellite in the geostationary orbit, the relative distance between the reflection point and receiver is small compared to the distance between the transmitter and receiver.
    - This allows for the assumption that the signals from the transmitter are parallel to each other at the reflection point and the receiver.

- The signal power received at the reflection point is approximately equal to the signal power received by the instrument.

2. There is high isolation between the sky-view antenna and the earth-view antenna. That is, the sky-view antenna mostly observes the direct signal from the transmitter, and the earth-view antenna mostly observes the reflected signals from the reflection point. It is assumed that there is less cross-contamination of signals between the antennas.

3. The reflection is specular. A wave reflection is considered to be specular if there is a single reflected ray path from the reflection point.

4. The RF system has a wideband, Gaussian, thermal noise from the amplifier chain, and the environment.

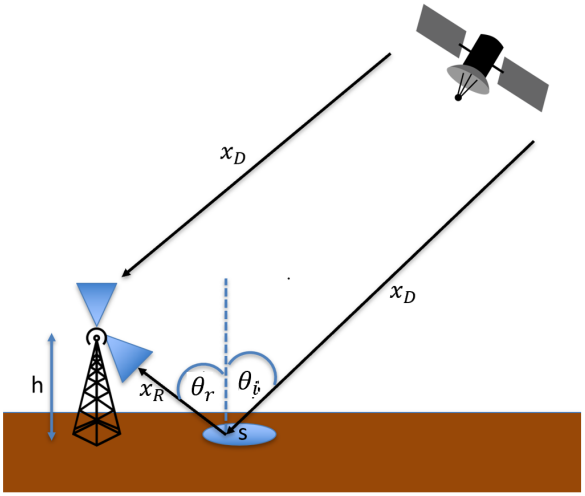

Figure 3.1. Basic geometry of the problem. The transmitter and receiver are located at some spatial distance. S is the reflection point. x_D is the direct signal and x_R is the reflected signal, assuming specular reflection

3.1.2 Specular reflection

By Snell's law of reflection, the incidence angle is equal to the reflected angle from a mirror-like surface; then, the reflection is considered to be specular [12]. Fig. 3.2 depicts the reflection from a smooth surface and a slightly rough surface.

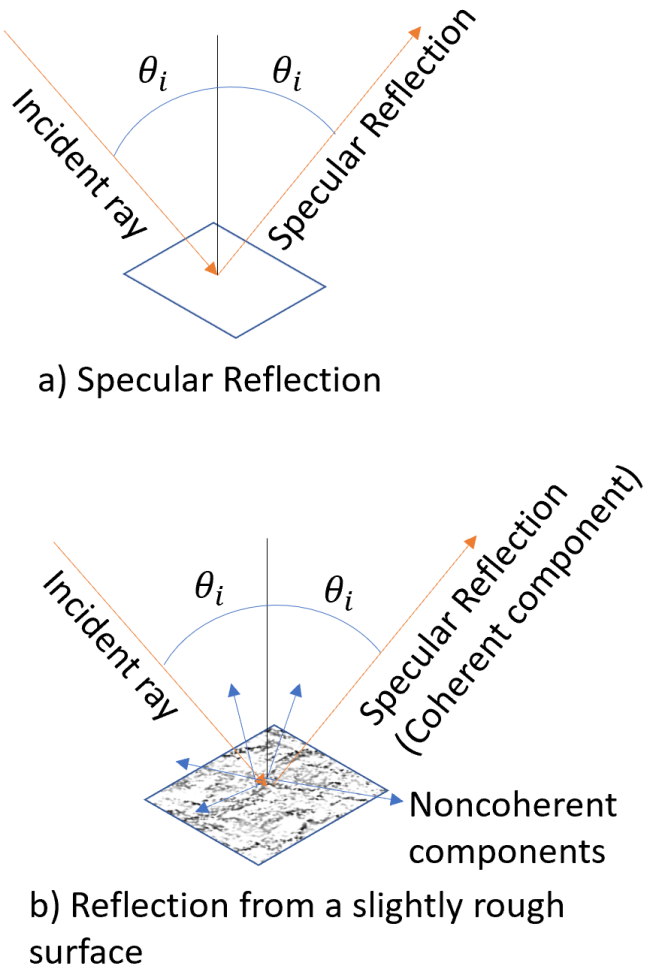

Figure 3.2. a) Specular reflection from a perfectly smooth surface b) The diffuse scattering pattern consists of a coherent component along the specular direction and a non-coherent component along all directions. The orange arrow represents specular coherent component and the blue arrows represent noncoherent components

Electromagnetically, the roughness of a surface is defined by the wavelength of the electromagnetic waves, λ. For a random surface with RMS (Root mean square) surface height, s the Rayleigh roughness criterion can be stated as follows:

$$s \leq \frac{\lambda}{8cos\theta_i} \tag{3.1}$$

Where s is the RMS surface height of the reflection point, λ is the wavelength of the incoming electromagnetic wave, and θ_i is the angle of incidence. The Rayleigh criterion is useful as a first-order classifier of surface roughness or smoothness. The Rayleigh roughness criterion states that the surface may be considered smooth if the phase difference between the reflected waves is less than $\pi/2$ radians, which is then considered to be a specular reflection.

The Rayleigh criterion value used in this experiment is presented in table 3.1. The elevation angle of the tower is 43.3°. Therefore, the incidence angle from the normal is 46.7°. The center frequency of S-band used in the experiment is 2.343125 GHz. Assuming the speed of light to be 299792458 m/s, the wavelength is 12.79 cm.

Table 3.1. Rayleigh Criterion Value

Signal	**Center Frequency**	**Wavelength**	**Rayleigh criterion**
S-Band	2.343125 GHz	12.79 cm	2.3312 cm

3.1.3 Fresnel zone

For specular reflection, i.e., the point where the incident and reflected angles are equal is the specular or reflecting point. This is the shortest distance between the transmitter and the receiver. The region surrounding the specular point, producing the reflection, is the Fresnel zone. For diffuse scattering, a large region of the surface around the Fresnel zone may re-radiate energy toward the receiver. This region is called the “glistening zone.” [16]. Multiple ellipses surround the specular point, each

one having distinct scatterometric properties. The Fresnel zone is depicted in Fig 3.1 as the ellipse on the soil, and the specular point is denoted by S.

The glistening zone may extend from the specular point to a wide area, depending on the surface roughness. Over this region, the incidence angle is assumed to be constant as the transmitting satellites are very far from the Earth, such that the incoming signals are approximately parallel to each other. Higher surface roughness leads to larger glistening zones and wider distribution in path delays from the transmitter-surface-receiver, thereby widening the shape of the waveform.

The ellipsoid of the Fresnel zone is defined by its semi-minor axis, b, and semi-major axis, a:

$$b = \sqrt{n\lambda \frac{d_1 d_2}{d_1 + d_2}} \tag{3.2}$$

where n is the Fresnel zone number, λ is the wavelength of signal, d_1 is the distance between the transmitter and specular point, and d_2 is the distance between the receiver the specular point.

For satellite-to-Earth link, $d_1 \approx d_1 + d_2$. Therefore,

$$b \approx \sqrt{n\lambda d_2} \approx \sqrt{\frac{\lambda h}{sin(\theta)}} \tag{3.3}$$

$$a = \frac{b}{sin(\theta)} \tag{3.4}$$

where h is the height of the receiver and θ is the elevation of the transmitter. For the experiment, the Fresnel zone semi-major axis is 3.5620 m and the semi-minor axis is 2.4429 m.

3.1.4 Penetration Depth

The penetration depth of electromagnetic waves is directly proportional to its wavelength and inversely proportional to the imaginary part of the dielectric constant

of the soil. Longer wavelengths penetrate the ground much better than shorter wavelengths. Hence, shorter wavelengths yield information about the upper layers [12]. Fig. 3.3 plots the penetration depth Vs. frequency for 5% and 30% soil moisture content [21]. The model used parameters of 0.4 for sand, 0.2 for clay and 0.4 for silt as the composition of the loam type soil. The vertical lines: 1) 370 MHz (MUOS), 2) 1.26 GHz (SMAP), 3) 1.575 GHz (GPS L1) and 4) 2.343 GHz (XM), represent the operating frequencies for various microwave instruments. It is noted that for dry soil, the penetration depth for the same frequency can be reasonably substantial as compared to wet soil.

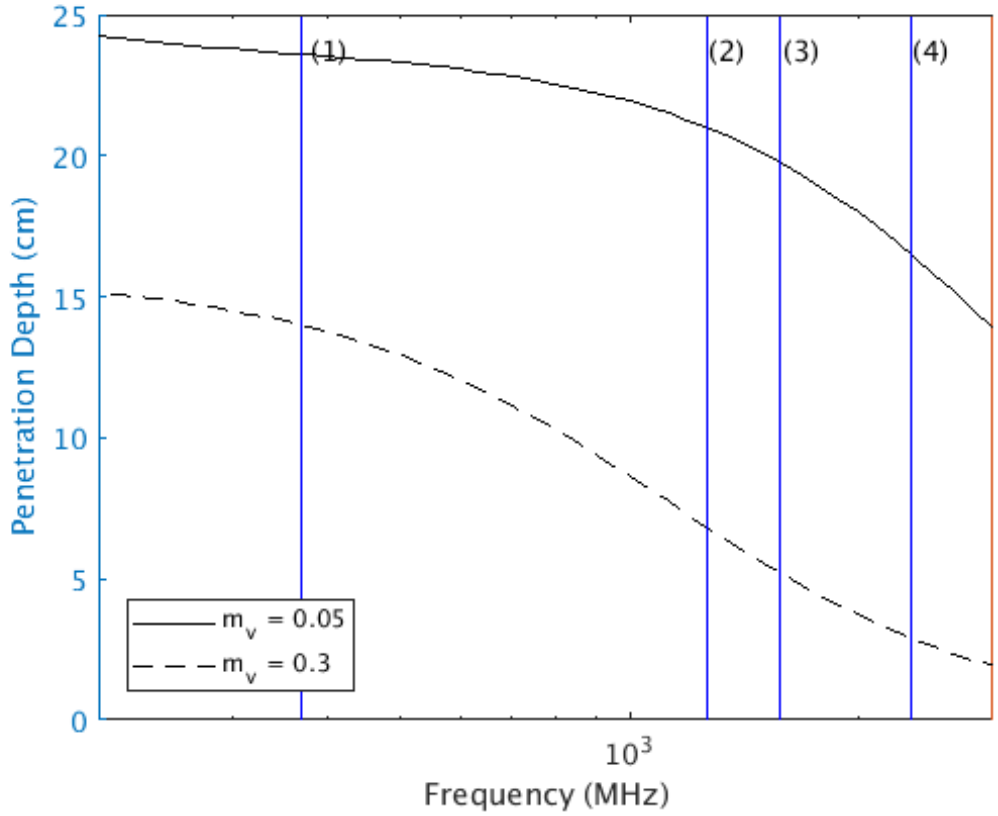

Figure 3.3. Soil Penetration Depth for Various Microwave Frequencies. [10]

3.1.5 Reflectivity

Reflectivity Γ is defined as the ratio of reflected (C_R) power to the incident or direct (C_D) power. It is the interaction of microwaves from the source of illumination with respect to the received microwaves, which are affected by the biomass and soil moisture. The reflection coefficient can be expressed as a complex number as determined by the Fresnel equations for a single layer, whereas the reflectivity is always a positive real number between 0 and 1.

$$\Gamma = \frac{C_R}{C_D} \tag{3.5}$$

3.2 Signal model

The basis of reflectivity is the understanding of how the electromagnetic wave changes as it reflects from any surface. In addition, the Fresnel coefficients relate to how the wave amplitude, phase, and polarization change as the wave reflects from the surface, and this is again dependent on the surface reflection properties. A single ray path model was used in this thesis for the reflectivity retrievals. The geometry of the signal model used is illustrated in Fig. 3.4.

Given a random signal with modulation $s(t)$, transmit power C, and carrier $e^{j\omega_C t}$, the transmitted signal can be modeled as:

$$x_T(t) = \sqrt{C}s(t)e^{j\omega_C t} \tag{3.6}$$

The direct signal at the sky-view antenna:

$$x_D(t) = \sqrt{C_D}s(t-\tau_D)e^{j(\omega_C(t-\tau_D)+\phi_D)} \tag{3.7}$$

Similarly, the reflected signal at the earth-view antenna:

$$x_R(t) = \sqrt{C_R}s(t-\tau_R)e^{j(\omega_C(t-\tau_R)+\phi_R)} \tag{3.8}$$

Where τ_D is the estimated time delay between the transmitter and the sky antenna, τ_R is the estimated time delay between the transmitter and the earth antenna

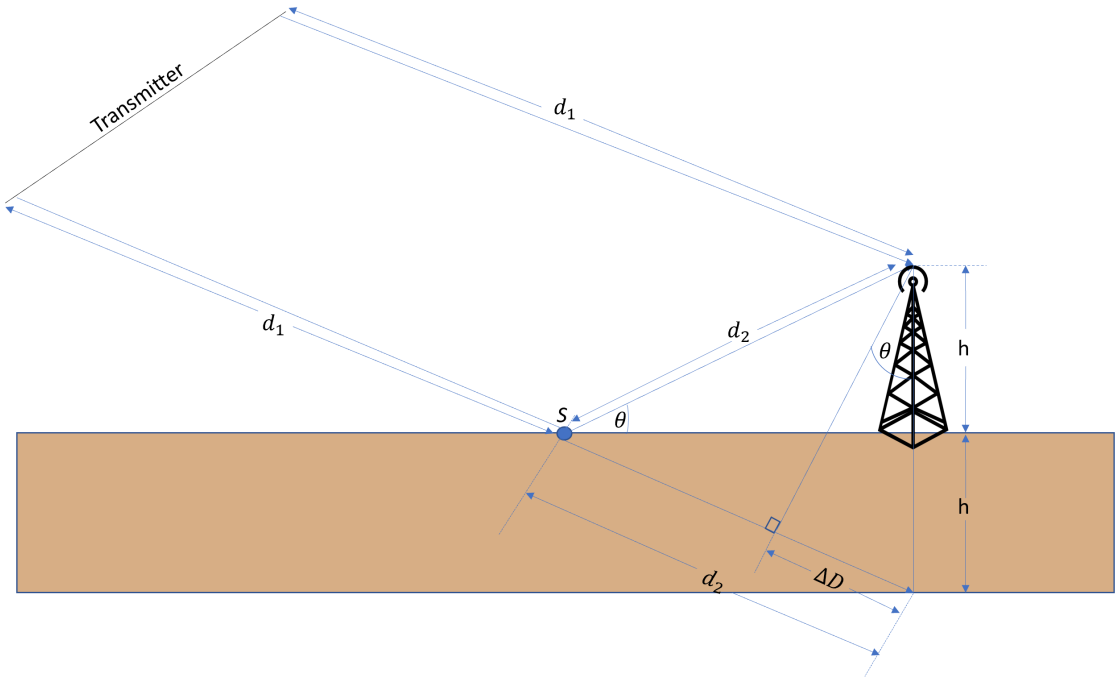

Figure 3.4. Geometry of the transmitter, receiver and specular point.

(including the time from the reflection point to the earth antenna), ϕ_D and ϕ_R are the direct and reflected phase differences, respectively. The spacial distance between the direct and reflected signal paths ΔD is:

$$\Delta D = 2hsin(\theta) \tag{3.9}$$

Where θ is the angle of elevation

$$\tau_R - \tau_D = \Delta\tau_{RD} = \frac{2hsin(\theta)}{c} = \frac{\Delta D}{c} \tag{3.10}$$

where c is the speed of light, $\Delta\tau_{RD}$ is the time delay (in sec) between the transmitted and the reflected signal.

3.3 Ambiguity Function

The ability of any radar system to distinguish between targets is governed by its range and Doppler resolution. Range resolution can be defined as the property to determine the distance between two closely-spaced targets. Doppler resolution is the ability to differentiate between the targets by virtue of the differing velocities of the signals. The cross-correlation function aids in evaluating the nature of the received signals which are effected by the target, attenuated due to power absorption and corrupted by noise. In our application, the scattering from the soil contains the soil moisture information which can be determined by ratio of cross-correlation and autocorrelation.

3.3.1 Autocorrelation

The autocorrelation of a signal is the correlation of a signal with a delayed copy of itself. Autocorrelation of the signal $x(t)$ is implemented for a finite integration time is as follows:

$$R_{xx}(\tau) = \frac{1}{T_I} \int_{T_I} x(t)x^*(t-\tau)dt \tag{3.11}$$

where T_I is the total finite integration time, x^* represents the complex conjugate of the signal and τ is the lag. This definition is also known as the "power-based" definition [36].

The average power of the signal can be written as

$$P_x = \frac{1}{T_I} \int_{T_I} |x(t)|^2 dt \tag{3.12}$$

It can be shown that evaluating the auto-correlation at lag = 0, gives the signal's average power:

$$R_{xx}(0) = \frac{1}{T_I} \int_{T_I} x(t)x^*(t-0)dt = \frac{1}{T_I} \int_{T_I} |x(t)|^2 dt = P_x \tag{3.13}$$

3.3.2 Cross-correlation

Cross-correlation is defined as the measure of similarity between two signals. For signals $x_1(t)$ and $x_2(t)$, cross-correlation is implemented for a finite integration time as follows:

$$R_{12}(\tau) = \frac{1}{T_I} \int_{T_I} x_1(t) x_2^*(t - \tau_{RD}) dt \tag{3.14}$$

3.3.3 Noise model

The received signal includes not only the transmitted signal, but also the noise emitted by the environment and generated in the radar hardware. This noise is undesirable. Over practical microwave bandwidths, the signal can be treated as wideband Gaussian white noise [12]. The power associated with this noise:

$$P_{thermal} = kT_eB \tag{3.15}$$

where k is Boltzmann's constant, T_e is the equivalent noise temperature in Kelvin, and B is the system noise bandwidth. The Power Spectral Density (PSD) of a random signal, such as noise, is the Fourier transform of the signal correlation function.

The microwave front-end applies an anti-aliasing filter of bandwidth B to the noise. The frequency response of this filter can be approximated by:

$$H(f) = \begin{cases} 1, & |f| \leq B \\ 0, & |f| > B \end{cases}$$

The Power Spectral Density (PSD) of the noise after applying the filter is then:

$$S_x(f) = \begin{cases} \frac{N_0}{2}, & |f| \leq B \\ 0, & |f| > otherwise \end{cases}$$

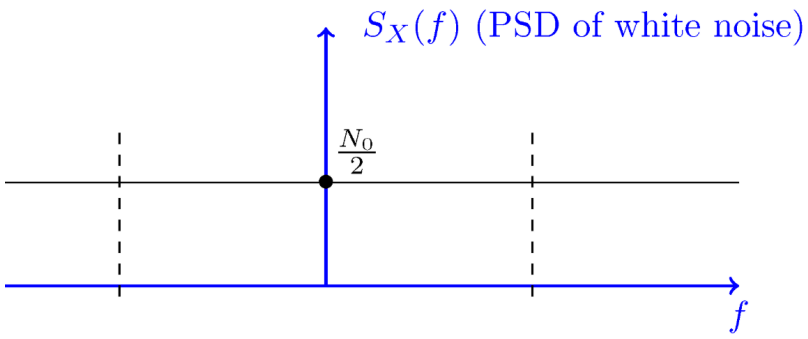

Figure 3.5. PSD of white noise

Total noise power:

$$P_n = \int_{-\infty}^{\infty} S_x(f)df = \frac{N_0}{2}\left[\int_{-B}^{B} 1df\right] = N_0 B \tag{3.16}$$

Also, autocorrelation of noise is given by:

$$R_n(\tau) = \mathcal{F}^{-1}\{S_x\} = \int_{\infty}^{\infty} \frac{N_0}{2} e^{j2\pi f\tau} H(f) = \frac{N_0}{2}\int_{-B}^{B} e^{2\pi\tau fj} df = N_0 \frac{sin(2B\pi\tau)}{2\pi\tau} \tag{3.17}$$

McNamee et. al [37] defined sinc function as:

$$sinc_\pi(x) = \begin{cases} 1, & x = 0 \\ \frac{sin(\pi x)}{\pi x}, & otherwise \end{cases}$$

Equating the power of band-limited thermal noise with the autocorrelation of the noise at zero-lag,

$$kT_e B = N_0 B \tag{3.18}$$

$$N_0 = kT_e \tag{3.19}$$

Therefore, the power of band-limited white additive Gaussian noise is:

$$P_n = R_n(\tau) = N_0 B sinc(2B\tau) = kT_e B sinc(2B\tau) \tag{3.20}$$

3.4 RF System model

All sources of noise in a microwave system can be converted into an equivalent noise temperature, T_e. The noise powers of the sky-view and earth-view antennas are represented by $\eta_{A,S}$ and $\eta_{A,E}$ and chosen equivalent brightness temperatures to be 2.7 K and 290 K, respectively [10].

The digital receiver has two inputs A and B and it performs the down conversion to baseband before the Analog to Digital (A to D) conversion. The signal as received by the digital receiver after down conversion in inputs A and B is modeled as:

$$x_A(t) = \sqrt{G_1}\big(\sqrt{G_{A,S}}x_D(t) + \eta_1(t)\big)e^{j(\omega_d t+\phi_d)} \tag{3.21}$$

$$x_B(t) = \sqrt{G_2}\big(\sqrt{G_{A,E}}x_R(t) + \eta_2(t)\big)e^{j(\omega_d t+\phi_d)} \tag{3.22}$$

Where ω_d is the down-convert frequency, ϕ_d is the accompanied down-convert phase, and η_1 and η_2 are the unknown noise sources in the channels. Using equations 3.7 and 3.8, the auto-correlation of the received signals, at input A:

$$R_{AA}(\tau) = G_1\Big(G_{A,S}C_D R_S(\tau)e^{j(\omega_C+\omega_d)\tau} + kT_1B_C sinc(2B_C\tau)e^{j\omega_d\tau}\Big) \tag{3.23}$$

Similarly for input B:

$$R_{BB}(\tau) = G_2\Big(G_{A,E}\Gamma C_D R_S(\tau)e^{j(\omega_C+\omega_d)\tau} + kT_2B_C sinc(2B_C\tau)e^{j\omega_d\tau}\Big) \tag{3.24}$$

The cross correlation between channels A and B:

$$R_{AB}(\tau) = \sqrt{G_1G_2}\Big(C_D\sqrt{G_{A,S}G_{A,E}\Gamma}R_S(\tau-\tau_{RD})e^{j(\omega_C+\omega_d)\tau}e^{-j((\omega_C\tau_{RD})-\phi_{RD})}\Big) \tag{3.25}$$

The random variables η_1 and η_2 are independent processes. The time difference: $\tau_{RD} = \tau_R - \tau_D$. The phase difference: $\phi_{RD} = \phi_R - \phi_D$

The model parameters are shown in Table 3.2.

Table 3.2. Model Parameters

Name	**Symbol**
Amplifier Gain of RF System 1	G_1
Amplifier Gain of RF System 2	G_2
Sky Antenna Gain	$G_{A,S}$
Earth Antenna Gain	$G_{E,S}$
System 1 Noise	η_1
System 2 Noise	η_2
Reflectivity	Γ
Sky Antenna Noise	$\eta_{A,S}$
Earth Antenna Noise	$\eta_{A,E}$
Matched Load noise	η_{ref}
Bandwidth of the signal	B_C

3.5 Calibration States

The microwave RF system has wideband thermal noise from the environment and amplifiers. The front end was designed with four states for system calibration: through, swap, load and phase . B_C is the bandwidth of the RF anti-aliasing filters in the digital receiver. The signals $x_A(t)$, $x_B(t)$ correspond to inputs A and B of the digital receiver after down conversion to baseband.

Through State

$$x_A(t) = \sqrt{G_1}(\sqrt{G_{A,S}}x_D(t) + \eta_{A,S}(t) + \eta_1(t))e^{j(\omega_d t+\phi_d)} \tag{3.26}$$

$$x_B(t) = \sqrt{G_2}(\sqrt{G_{A,E}}x_R(t) + \eta_{A,E}(t) + \eta_2(t))e^{j(\omega_d t+\phi_d)} \tag{3.27}$$

Performing the autocorrelations and cross-correlations:

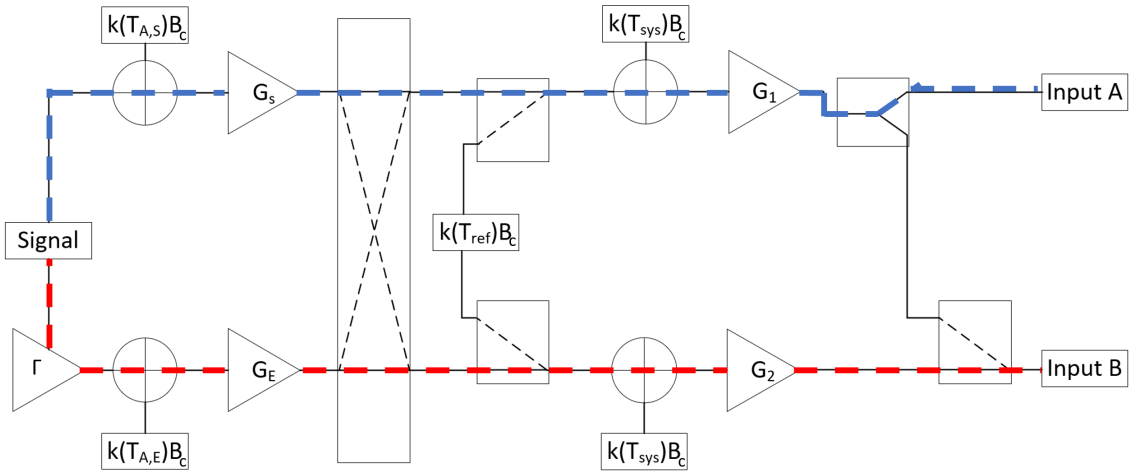

Figure 3.6. Through State

$$R_{AA}^{T}(\tau) = G_1\Big(G_{A,S}C_D R_S(\tau)e^{j(\omega_C+\omega_d)\tau} + ((T_{A,S}+T_1)kB_C sinc(2B_C\tau))e^{j\omega_d t}\Big) \quad (3.28)$$

$$R_{BB}^{T}(\tau) = G_2\Big(G_{A,E}\Gamma C_D R_S(\tau)e^{j(\omega_C+\omega_d)\tau} + ((T_{A,E}+T_2)kB_C sinc(2B_C\tau))e^{j\omega_d t}\Big) \quad (3.29)$$

$$R_{AB}^{T}(\tau) = \sqrt{G_1G_2}\Big(C_D\sqrt{G_{A,S}G_{A,E}\Gamma}R_S(\tau-\tau_{RD})e^{j(\omega_C+\omega_d)\tau}e^{-j(\omega_C\tau_{RD}-\phi_{RD})}\Big) \quad (3.30)$$

Swap

The transfer switch was used to swap the amplifiers between the sky-view and earth-view antenna.

$$x_A(t) = \sqrt{G_1}(\sqrt{G_{A,E}}x_R(t) + \eta_{A,E}(t) + \eta_1(t))e^{j((\omega_d t)+\phi_d)} \quad (3.31)$$

$$x_B(t) = \sqrt{G_2}(\sqrt{G_{A,S}}x_D(t) + \eta_{A,S}(t) + \eta_2(t))e^{j((\omega_d t)+\phi_d)} \quad (3.32)$$

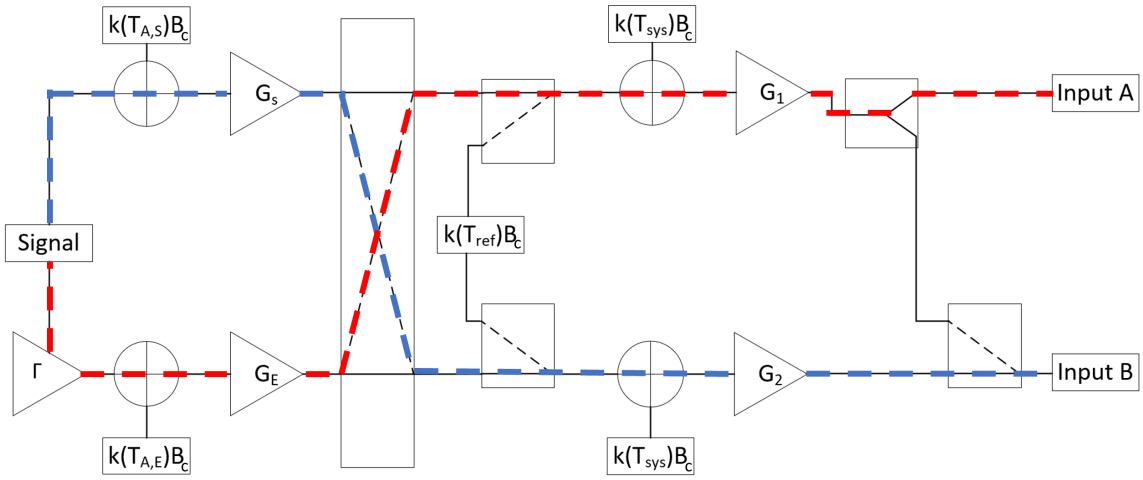

Figure 3.7. Swap State

Performing the autocorrelations and cross-correlations for the swap state:

$$R^S_{AA}(\tau) = G_1\Big(G_{A,E}C_D\Gamma R_S(\tau)e^{j(\omega_C+\omega_d)\tau} + ((T_{A,E}+T_1)kB_C sinc(2B_C\tau))e^{j\omega_d t}\Big) \quad (3.33)$$

$$R^S_{BB}(\tau) = G_2\Big(G_{A,S}C_D R_S(\tau)e^{j(\omega_C+\omega_d)\tau} + ((T_{A,S}+T_2)kB_C sinc(2B_C\tau))e^{j\omega_d t}\Big) \quad (3.34)$$

$$R^S_{AB}(\tau) = \sqrt{G_1G_2}\Big(C_D\sqrt{G_{A,S}G_{A,E}}\Gamma(R_S(\tau-\tau_{RD})e^{j(\omega_C+\omega_d)\tau}e^{-j((\omega_C\tau_{RD})-\phi_{RD})}\Big) \quad (3.35)$$

Load

Reflective switches were used to switch in matched loads into the receiver chains. The uncorrelated noise source between the two channels, η_{ref} is generated by separate matched loads in each receiver chain. In each amplifier T_{ref} is the temperature of the matched load which was recorded with a Resistance Temperature Detector RTD

temperature sensor. The η_{ref} is independent noise sources in channel A and B. However, the match loads have the same noise power as they were both the same temperature (connected via copper wire).

$$x_A(t) = \sqrt{G_1}\Big(\eta_{ref}(t) + \eta_1(t)\Big)e^{j(\omega_d t + \phi_d)} \tag{3.36}$$

$$x_B(t) = \sqrt{G_2}\Big(\eta_{ref}(t) + \eta_2(t)\Big)e^{j(\omega_d t + \phi_d)} \tag{3.37}$$

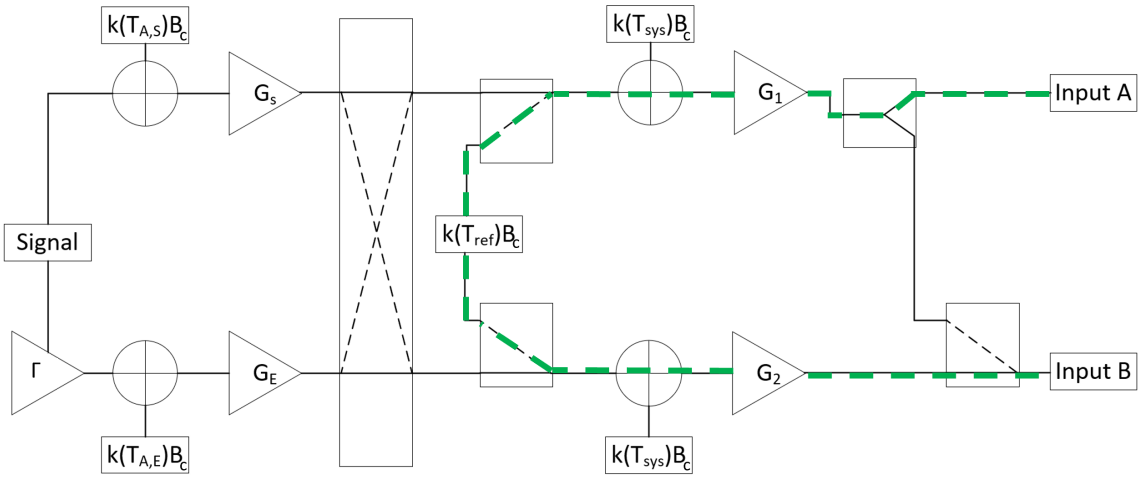

Figure 3.8. Load State

Performing the autocorrelations and cross-correlations for the load state:

$$R^L_{AA}(\tau) = G_1\Big((T_{ref} + T_1)kB_C sinc(2B_C\tau)e^{j\omega_d\tau}\Big) \tag{3.38}$$

$$R^L_{BB}(\tau) = G_2\Big((T_{ref} + T_2)kB_C sinc(2B_C\tau)e^{j\omega_d\tau}\Big) \tag{3.39}$$

$$R^L_{AB}(\tau) = 0 \tag{3.40}$$

Phase

The sky-view antenna and the amplifier chain 1 were connected to both inputs A and B. This was added to verify that the phase of the two input channels of the digital receiver were synchronized. This calibration state was used only in the 2018 experiment for 2 seconds after the swap state.

$$x_A(t) = \sqrt{G_1}(\sqrt{G_{A,S}}x_D(t) + \eta_{A,S}(t) + \eta_1(t))e^{j(\omega_d t + \phi_d)} \tag{3.41}$$

$$x_B(t) = \sqrt{G_1}(\sqrt{G_{A,S}}x_D(t) + \eta_{A,S}(t) + \eta_1(t))e^{j(\omega_d t + \phi_d)} \tag{3.42}$$

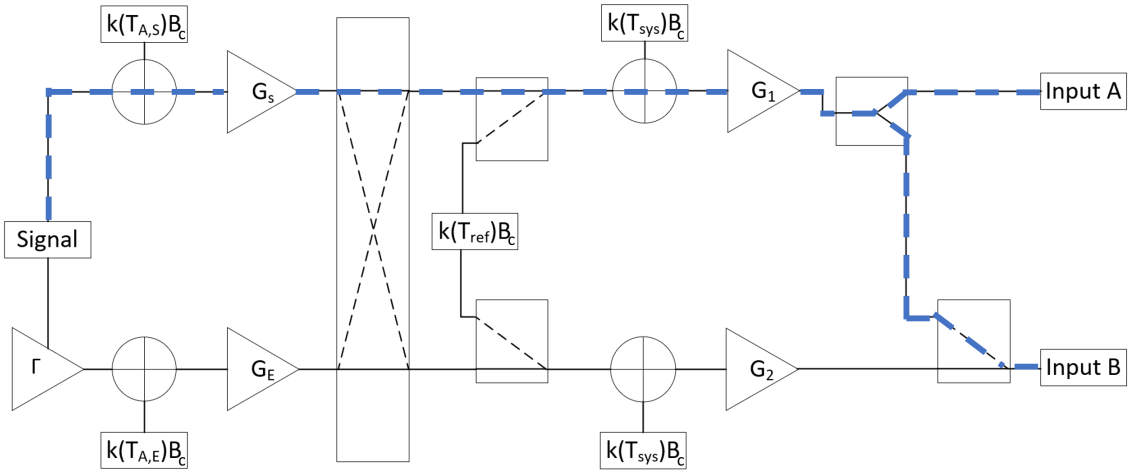

Figure 3.9. Phase State

If $x_A(t)$ and $x_B(t)$ are phased synchronized, then:

$$R^P_{AB}(\tau) = G_1\Big(G_{A,S}C_D R_S(\tau)e^{j(\omega_C+\omega_d)\tau} + ((T_{A,S}+T_1)kB_C sinc(2B_C\tau))e^{j\omega_d t}\Big) \tag{3.43}$$

3.6 Reflectivity

The reflectivity can be estimated from the ratio of cross-correlations and auto-correlations of the signals along direct and reflected paths with noise calibrations in consideration. Using the autocorrelation from the load state and the autocorrelation of the mean noise floor in the through state, we have the gain of channel 1:

$$G_1 = \frac{\left(R^L_{AA}(\tau) - R^{T_{Noise}}_{AA}(\tau)\right)}{\left(T_{ref} k B_C sinc(2B_C\tau)\right)} \tag{3.44}$$

At $\tau = 0$,

$$G_1 = \frac{\left(R^L_{AA}(0) - R^{T_{Noise}}_{AA}(0)\right)}{\left(T_{ref} k B_C\right)} \tag{3.45}$$

Similarly, the gain of channel 2:

$$G_2 = \frac{\left(R^L_{BB}(0) - R^{T_{Noise}}_{BB}(0)\right)}{\left(T_{ref} k B_C\right)} \tag{3.46}$$

Now, we obtain T_1 using equation 3.28 and 3.45

$$T_1 = \frac{R^L_{AA}(0)}{G_1 k B_C} - T_{ref} \tag{3.47}$$

Substitute T_1 in equation 3.28 to obtain C_D

$$C_D = \frac{\frac{R^T_{AA}(0)}{G_1} - k B_C (T_{AS} + T_1)}{G_{AS}} \tag{3.48}$$

Substituting the values of G_1, G_2, C_D in equation 3.30,

$$\sqrt{\Gamma} = \frac{R^T_{AB}(\tau_{RD})}{C_D \sqrt{G_1 G_2 G_{AS} G_{AE}}} \tag{3.49}$$

4. DATA PROCESSING

The sampled XM data was recorded by the sky-view antenna and the earth-view antenna. The data was recorded in Eastern Standard Time (EST) for all the experiments. A block of 60 seconds of data was recorded every 30 minutes for the 2017 experiment and every 15 minutes for the 2018 experiment. The sampling rate for both the data campaigns was 8 MHz. However, 8 bits quantization was used in both real and imaginary parts for the 2017 experiment and 12 bits quantization bits for both real and imaginary parts for the 2018 data campaign. The recording parameters are summarized in Table 4.1.

Table 4.1. Recording Parameters for the 2017 and 2018 experiments

Recording Parameter	**2017**	**2018**
Date	May 26, 2017 - Jun 07, 2017	Jun 09, 2018 - Jun 26, 2018
Periodicity	30 minutes	15 minutes
Duration	60 seconds	60 seconds
Center frequency	2.343125 GHz	2.343125 GHz
Sampling frequency	8 MHz	8 MHz
Quantization	8 bits, imaginary and real	12 bits, imaginary and real

The data was recorded for both XM-3 frequencies and XM-4 frequencies centered at 2.343125 GHz. The signal is down-sampled to baseband in the USRP with an in-phase and a quadrature component (the real and the imaginary components of the signal) and then passed through a digital lowpass filter of bandwidth 1.64 MHz in order to isolate the XM-3 and XM-4 bands separately to filter noise and potential interference. The noise bands are also filtered as higher-end noise band and lower-end noise band separately, on either side of the required channel spectrum. The lowpass

filter was designed in MATLAB and the frequency response shown in Fig. 4.1. The script used is attached in Appendix B.

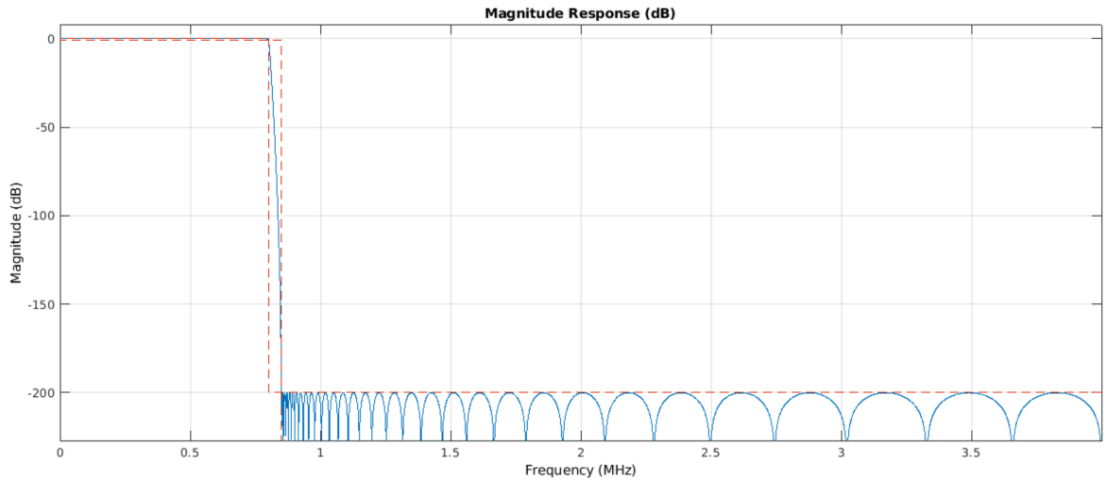

Figure 4.1. Frequency response of the digital filter used. The pass frequency is 1.6 MHz and the stop frequency is 1.7 MHz. The amount of ripple in pass band is 1 dB and in stop band is 200 dB

The numerically efficient method of Fast Fourier Transform (FFT) and Inverse Fast Fourier Transforms (IFFT) is applied to the filtered channel bands and noise bands. The autocorrelation is performed by the FFT of the channel with its complex conjugate, and cross-correlation is performed by the direct and reflected filtered channels, followed by the IFFT of it. For the power-based definition, this equation is averaged for the integration time or the number of samples. It is represented as follows:

$$R_x = \frac{1}{samples}\left[IFFT(FFT(x_D(n)).FFT(x_R^*(n)))\right] \tag{4.1}$$

Welch Power Spectrum estimate was used in MATLAB to plot the PSD of the direct and the reflected signals. The unfiltered direct and the reflected PSD in the through state are shown in the top two subplots of Fig. 4.2. The filtered XM-3 frequencies are shown in the bottom two subplots. It is noted that 8 MHz is the

sampling bandwidth of recorded direct and reflected signals. The bandwidth of the channel of interest is 1.64 MHz.

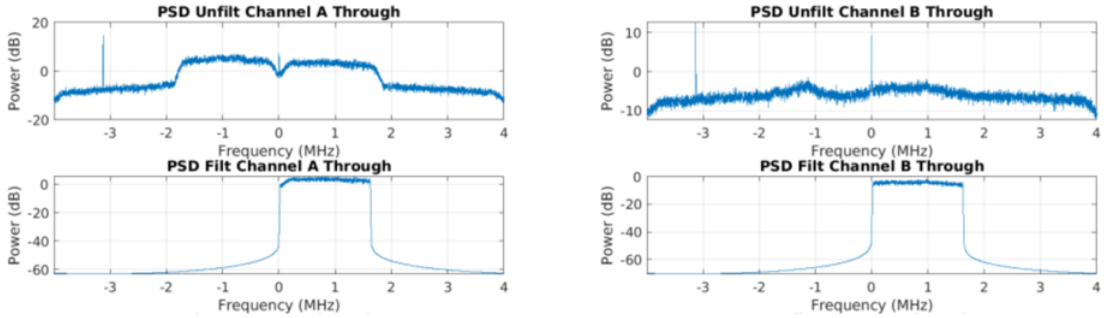

Figure 4.2. The PSD of the direct and reflected signals at input A and B of the USRP. The unfiltered direct and reflected signals are plotted in the top two plots. The filtered channel (XM-3) frequencies are plotted in the bottom two plots.

There is a peak at 3.125 MHz on the left hand side of the XM-4 channel. This spike appears in all the plots of all the states during data processing for both the 2017 and 2018 data, and it could be due to an internal spike at the USRP.

4.1 Correlations and state parsing

The autocorrelation of the direct and the reflected signals is shown in Fig. 4.3. It is noted that the autocorrelation and the cross-correlation values lie between 0 and 1. It is observed that the peak of the direct and reflected autocorrelation values have a greater magnitude than the cross-correlation peak as expected. The SAF function is a sinc function as expected with the peak lying at the sample of 0 lag, i.e., $\tau = 0$, which is the 80001^{st} sample.

The autocorrelation and cross-correlations of the direct signal, reflected signal, the lower-end noise band, and higher-end noise bands are calculated for 20 seconds (minimum duration for periodic repetition of all 3 calibration states). Since the states are not identified during the recording process, they are determined in the

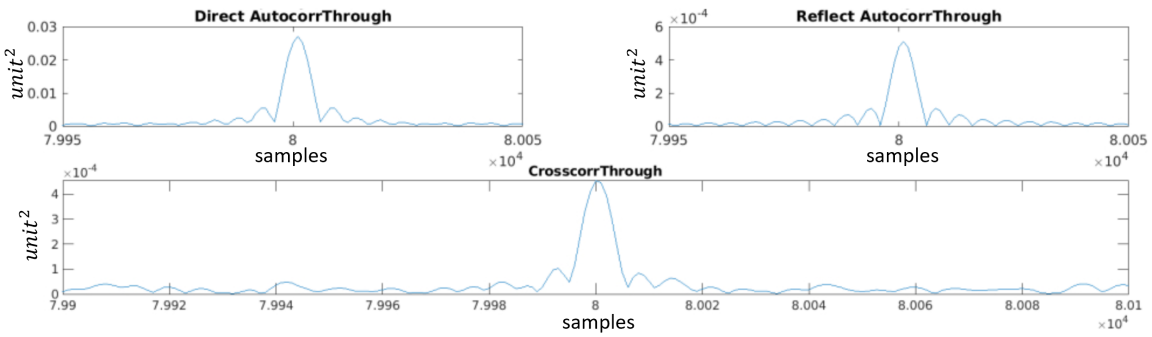

Figure 4.3. Top subplots: The autocorrelation of direct and reflected signals. Bottom subplot: The cross-correlation of the direct and reflected signals

post-processing of the data. The window-length of integration time is chosen to be 20 ms. That is, 160000 samples are recorded every 20 ms as the sampling rate is $8 * 10^6$ samples per second. A specific state parser script is written for the 2017 and 2018 XM signals which determine the various states. A typical plot of autocorrelations at lag=0 and cross-correlations at τ_{RD} VS. time is plotted in Fig. 4.4. The corresponding state identification and verification plot is shown in Fig. 4.5. Fig. 4.4 and 4.5 correspond to data processing of XM-3 signals for Jun 09, 2018, 03:45 (File name 20180609T034500Z).

The data processing parameters are summarized in the Table 4.2.

Table 4.2. Data Processing parameters for the 2017 and 2018 experiments

Parameter	**2017**	**2018**
Sampling frequency	8 MHz	
Window Length	20 ms	
Number of samples	80000 each, imaginary and real	
Total integration time	20 sec	
Path delay	37.47 m	

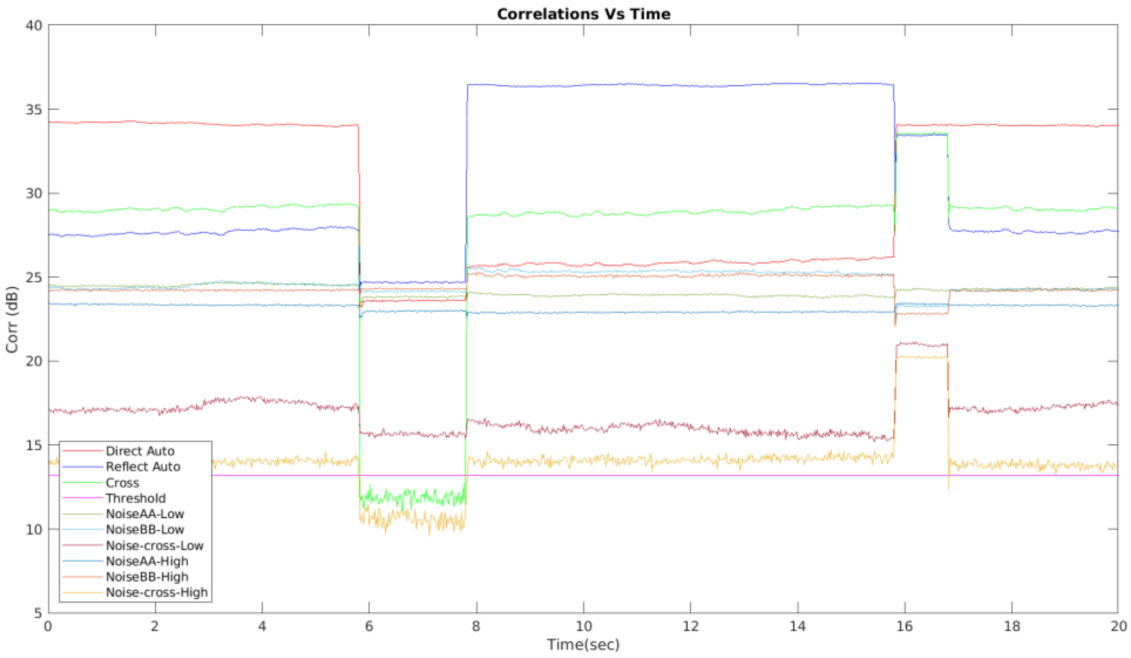

Figure 4.4. Autocorrelations and cross-correlations of direct, reflected, lower-end noise and upper-end noise signals. The correlations are converted to dB for ease of understanding. X-axis represents the time in seconds and y-axis represents the correlation power in dB. The plot is for the file 20180609T034500Z.

4.2 RFI and other anomalies

4.2.1 RFI

The cases of unusual high RFI is noted in the lower-end noise bands during certain times of the day. This source of RFI is identified to be from a terrestrial repeater of SDARS. The source of the RFI could also be the noise from the microwave hardware system, although it is unsure why it shows up as high-frequency noise during certain times. It is noted that this RFI activity is observed only from 00:00 to 10:00. It is present mostly during the night-times for the entire course of both the data campaigns of 2017 and 2018. The times are in EST, also correspond to the time when the data was recorded.

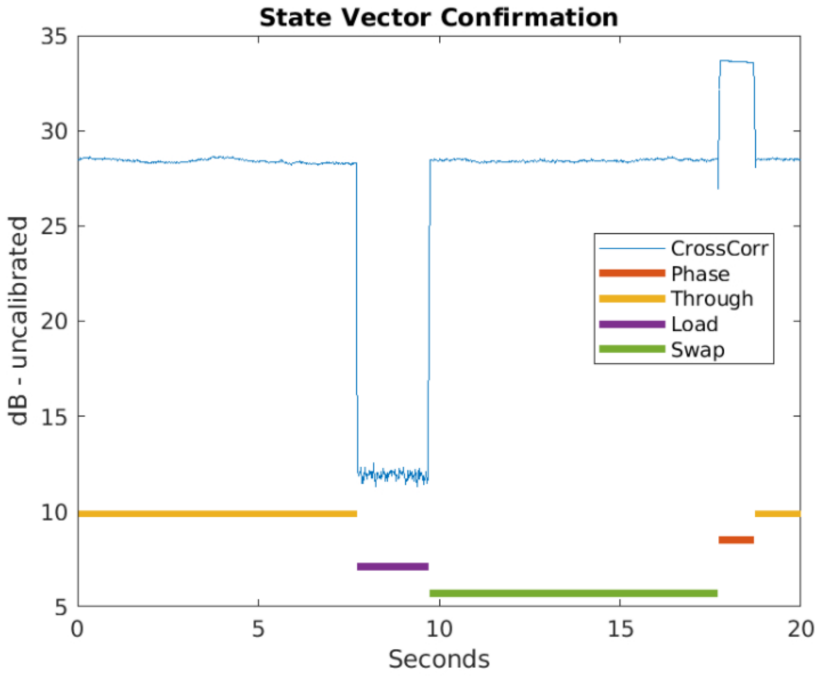

Figure 4.5. Confirmation of states parsed during data-processing. The legend indicates the colour of each state and the corresponding state identification is on the x-axis in the plot. The plot is for the file 20180609T034500Z.

Fig. 4.6 illustrates the PSD for the RFI case for file Jun 14, 2018, 04:15 for XM-3 signal processing. Due to the presence of the RFI, the power of the channels under study (XM-3 and XM-4 frequencies) also increases, thereby increasing the magnitude of autocorrelation and cross-correlation of the noise bands and the channels. This results in an abrupt increase in reflectivity which is independent of soil moisture. The presence of RFI is identified in the data as an increase in the magnitude of cross-correlation present in the lower-end noise bands.

Filtering out RFI

For the application of digitally filtering the RFI, a threshold is set such that the cross-correlation of the lower-end noise bands does not exceed a certain value. By this method, RFI is identified and digitally filtered.

$$threshold = 0.0011(dB)$$
$$R_{AB}{}^{Noise} > threshold \tag{4.2}$$

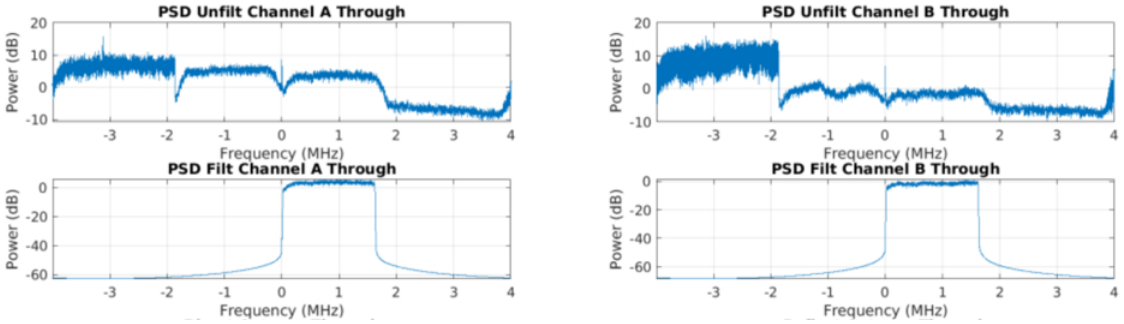

Figure 4.6. PSD of unusual RFI found in the file 20180614T041500Z. The high frequency modulations on the lower-end noise band can be compared to Fig. 4.2 where the RFI is not present.

4.2.2 Specular Point tracking

The peak of the cross-correlation lies between two discrete samples of time. The path delay corresponds to 43.89 m, whereas the discrete samples are collected every 37.47 m. To obtain the peak value of cross-correlation at τ_{RD}, the time-shifting property of Fourier transform is implemented. A shift in time corresponds to a phase rotation in the frequency domain. This property of Fourier Transforms is used to find the cross-correlation at values smaller than the sample size by multiplying the Fourier transform with a phase rotation in the frequency domain.

The time-shifting property of Fourier Transform used is as follows:

$$\begin{aligned}\mathcal{F}\{g(t-a)\} &= \int_{-\infty}^{\infty} g(t-a)e^{-j(2\pi ft)}dt \\ &= \int_{-\infty}^{\infty} g(u)e^{-j(2\pi f(u+a))}du \\ &= e^{-j(2\pi fa)}\int_{-\infty}^{\infty} g(u)e^{-j(2\pi fu)}du \\ &= e^{-j(2\pi fa)}\mathcal{G}(f)\end{aligned} \tag{4.3}$$

The time difference between two samples is discretized further by choosing frequencies such that the number of elements remains the same for the direct and reflected signals. The increment in frequencies corresponds to 50Hz, which is 0.745 m, in distance. The time delay, τ_{RD} is given by:

$$\tau_R - \tau_D = \Delta\tau = \frac{2hcos(\theta)}{c} \tag{4.4}$$

where c is the speed of light, h is the height of the tower and θ is the elevation angle.

The specular point is essentially tracked by changing the frequency and the delay so as to accurately locate the peak for the cross-correlation. For each frequency change, the peak is maximized for all the delays, which is a fraction between two samples. The FFT of the reflected signal is multiplied by the shift in frequencies as concluded from equation 4.3. The cross-correlation values are stored for all the delays and frequencies. The maximum value of the cross-correlation function is chosen such that the difference in τ_{RD} and the delay obtained is minimum.

4.2.3 Multi-peaks in the cross-correlations

The cross-correlation function for the direct and reflected signals has a single peak at the path delay. There is a certain bit of asymmetry in the cross-correlation function, due to the information present in the reflected waveform. This is observed in Fig. 4.3. However, there were multiple cases of multi-peaks and highly asymmetric cross-correlation functions. This could be due to imperfect isolation between the

direct and the reflected antennas, which contaminated the signal ray paths. In all the cases of multi-peaks observed in the cross-correlation function in the 2017 and 2018 experiments, it is observed that all the multi-peaks which occur in the through state (i.e., direct signal into Input A of the USRP and reflected signal into Input B of the USRP), also occur in the swap state where the antennas are flipped with respect to the inputs of the USRP. Two such cases of highly asymmetric multi-peaks observed in the through state and the swap state processing are presented in Fig. 4.7 and Fig. 4.8. It is noted that the through and swap cross-correlations are mirror images of each other with respect to $\tau = 0$ ($80001^s t$ sample). This implies that the assumption of ideal isolation of the sky-view antenna and the earth-view antenna is inaccurate.

The cross-correlation magnitude are not normalized in this case. The cross-correlations are performed for the file Jun 25, 2018, 22:00.

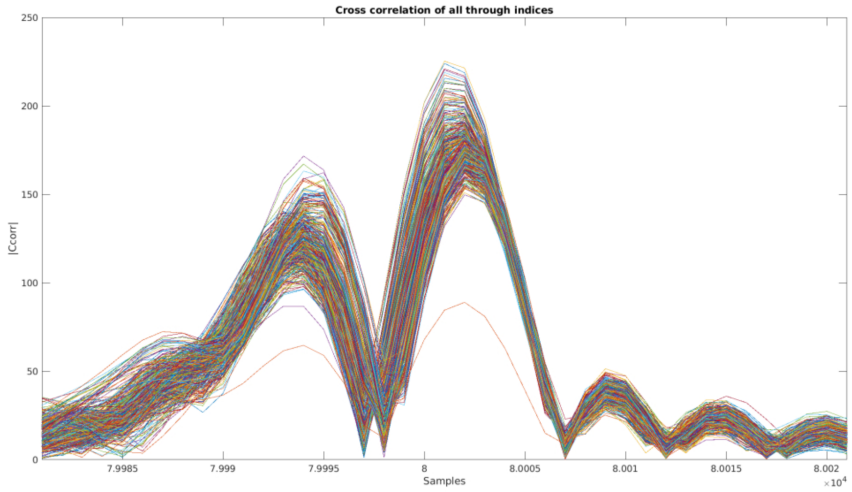

Figure 4.7. Cross-correlation of all the through state indices

Filtering out the asymmetry

For all the through indices, the cross-correlation is found by applying a filter to use only those through indices which do not have multi-peaks or the asymmetry. This is done by taking the mean of cross-correlation values of the 20 samples on either side

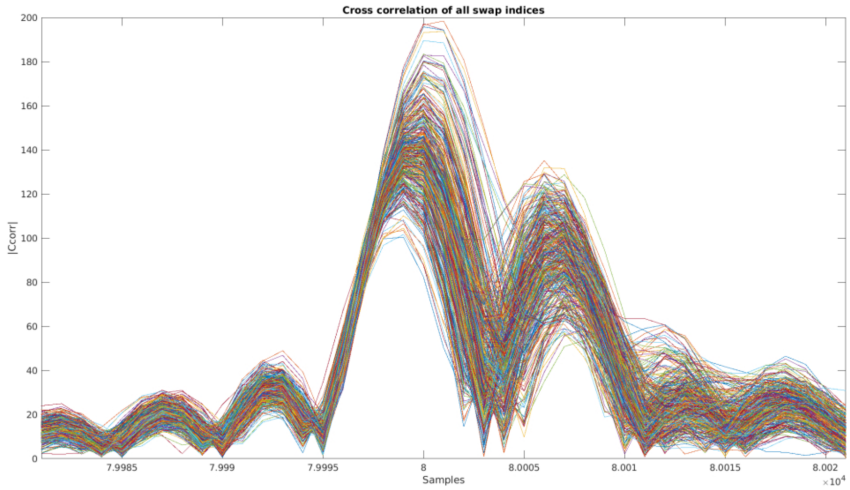

Figure 4.8. Cross-correlation of all the swap state indices

of the peak. If the average is 22.5% of the peak value, then that through index is chosen for further calculations. This process can be described as follows in the script for filtering multi-peaks:

$$\begin{aligned} \bar{R}^{-}_{AB} &\leq 22.5\% R_{ABmax} \\ \bar{R}^{+}_{AB} &\leq 22.5\% R_{ABmax} \end{aligned} \tag{4.5}$$

If there are no such through indices, then the entire file is skipped and the mean values are for the correlations for such asymmetric files are stored as-is. However, such files are marked and not used for reflectivity calculations. Fig. 4.9 presents with the cross-correlation results with the through state indices after filtering out asymmetry for the same file Jun 25, 2018, 22:00.

4.2.4 Phase of the cross-correlation

For the 2017 experiment, the phase of the cross-correlations was plotted with respect to time. Wind speeds during the time of data recording were plotted alongside, to observe the relationship between wind speeds and the phase of cross-correlation.

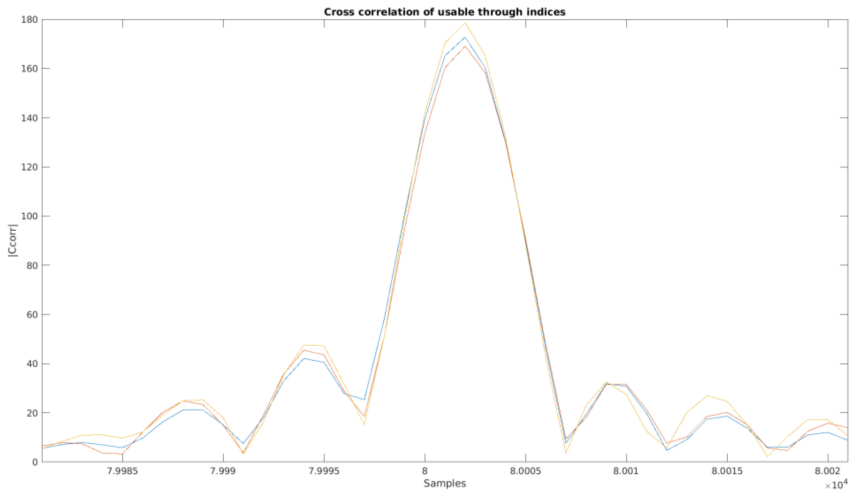

Figure 4.9. Cross-correlation of all the through state indices filtered of the asymmetry

Since the phase was sinusoidal in nature, it was presumed that the physical movement of the tower at 32 m high, could result in such behaviour. However, no such relationship could be established with respect to the physical movement of tower due to high wind speeds with the sinusoidal nature of the phase of cross-correlation. Fig. 4.10 (file 20170526T180000Z) and 4.11 (file 20170604T153000Z) represent phase of cross-correlation with respect to time along with same wind speed of 3.1 m/s but different sinusoidal behaviours.

4.2.5 Reflectivity retrieval

Another script was written to use all the correlation values saved in a .mat file from the raw data processing. Using equation 3.49, the cross-correlation values obtained after filtering RFI and asymmetry are used for the cross-correlation in the through state. All the autocorrelations and cross-correlations are averaged for that particular state for the channels, lower-end, and higher-end noise bands. The noise floor calibration is performed using higher-end noise bands since the RFI is evidently present in the lower-end noise bands. The reflectivities obtained are plotted with respect to

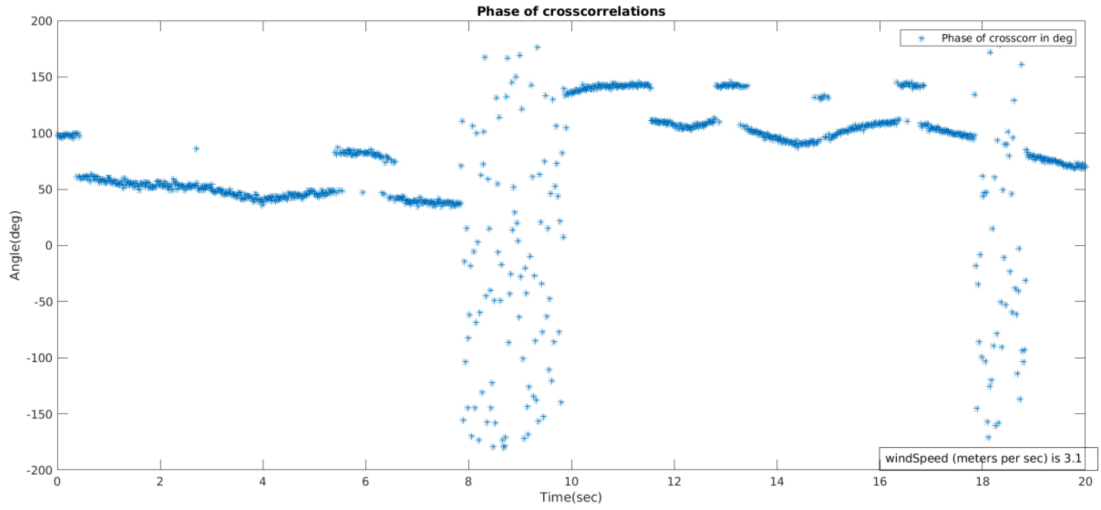

Figure 4.10. Phase of cross-correlation with respect to time with wind speed of 3.1 m/s for the file 20170526T180000Z

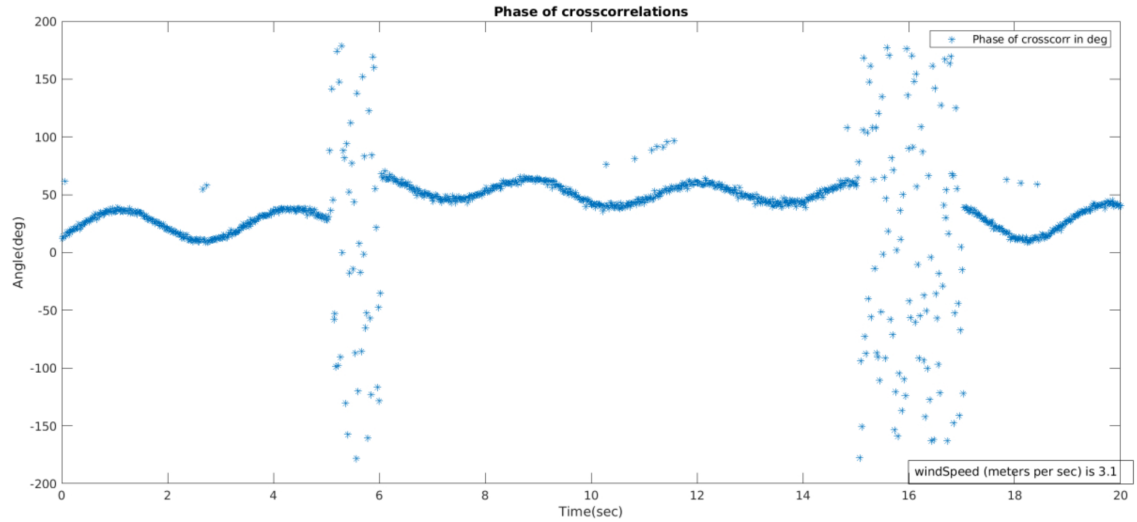

Figure 4.11. Phase of cross-correlation with respect to time with wind speed of 3.1 m/s for the file 20170604T153000Z

the in-situ soil moisture data from the HydraProbes at 5 cm. All the HydraProbe reading used in this thesis were from the half-tile location of the HydraProbes for

both the 2017 and 2018 experiments. The trend of the reflectivities with the SMC is also plotted. These values are also compared to the SCoBi [38] model.

5. REFLECTIVITY RETRIEVAL RESULTS

In this chapter, the results obtained for the 2017 and 2018 S-band tower-based SoOp experiments are presented. The raw data processing script, mentioned in Appendix B was used for autocorrelations and cross-correlations of XM-3 and XM-4 channels separately, along with the autocorrelations and cross-correlations of lower-end and higher-end noise bands for the 2017 and 2018 experiments.

5.1 2017 results

5.1.1 Comparison with In-situ SMC

The data was saved separately for XM-3 and XM-4 frequencies as .mat files. The reflectivity values are plotted against time and the soil moisture content (SMC) obtained from the HydraProbes at 5 cm. The diurnal effect captured by the reflectivity can be observed, despite the presence of RFI cases during the night.

Reflectivity VS. SMC for XM-3 and XM-4 frequencies are plotted in Fig. 5.2. It is expected that higher SMC relates to higher reflectivity values. However, due to the presence of RFI, reflectivity values are higher, independent of soil moisture. Therefore, RFI filtering is necessary for accurate results. Despite the presence of RFI, a thick cluster of smaller reflectivities values is observed for lower SMC values.

The RFI is digitally filtered from the data by setting a threshold such that the lower-end noise floor cross-correlation values do not exceed 0.0011 dB. This factor is chosen since the PSD of non-RFI cases can be visually verified with the cross-correlation of lower-end noise bands. Furthermore, the reflectivity values are averaged every three files (1.5 hours, since each file is recorded 30 minutes apart), to provide a smooth transition in the reflectivities. The SMC VS reflectivity values are plotted for

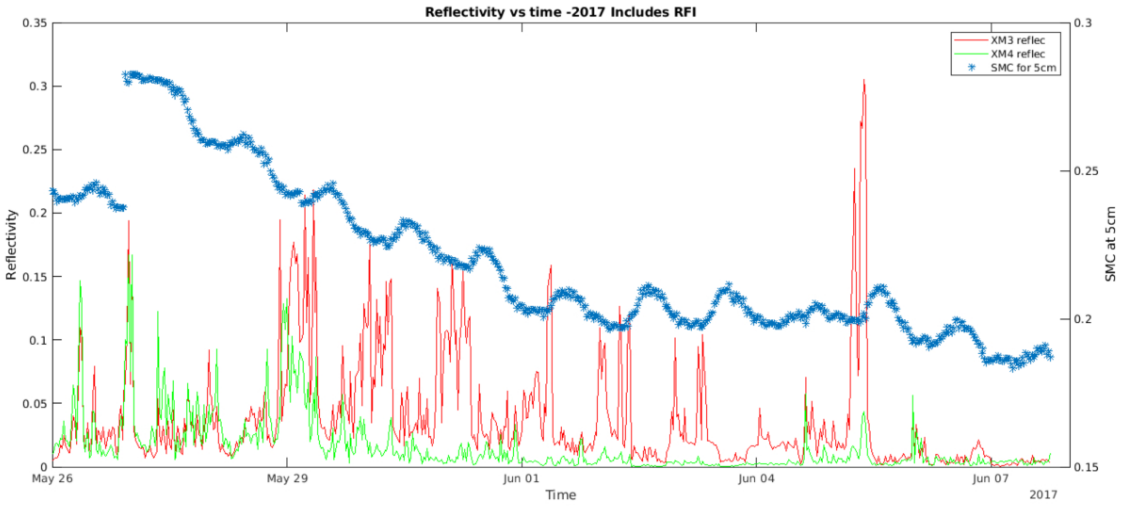

Figure 5.1. Reflectivity VS. SMC at 5 cm with respect to time. This is the preliminary result as the retrievals contain the effects of RFI. The right-hand side y-axis represents the volumetric soil moisture content. The left-hand side y-axis represents the reflectivity retrieval from the experiment. The x-axis represents the duration of the experiment conducted from 05/26/2017,00:00 to 06/07/2017,18:00.

the averaged reflectivities after digitally filtering out RFI from the data. The trend of higher SMC relating to higher reflectivity value can be observed in Fig. 5.4.

5.1.2 Comparison with SCoBi model [38]

Boyd et al. [38] from the IMPRESS Lab, Department of Electrical and Computer Engineering, Mississippi State University have been working on a Signals of Opportunity (SoOp) Coherent Bistatic (SCoBi) simulator. It simulates the direct and specular reflection contributions on the bistatically received signals. It is released with a set of built-in plotting functions. The simulator has various capabilities for polarizations, different antenna patterns, biomass, and multi-layer soil analysis, etc. Three soil moisture profile fit functions are used to capture potential changes in surface soil

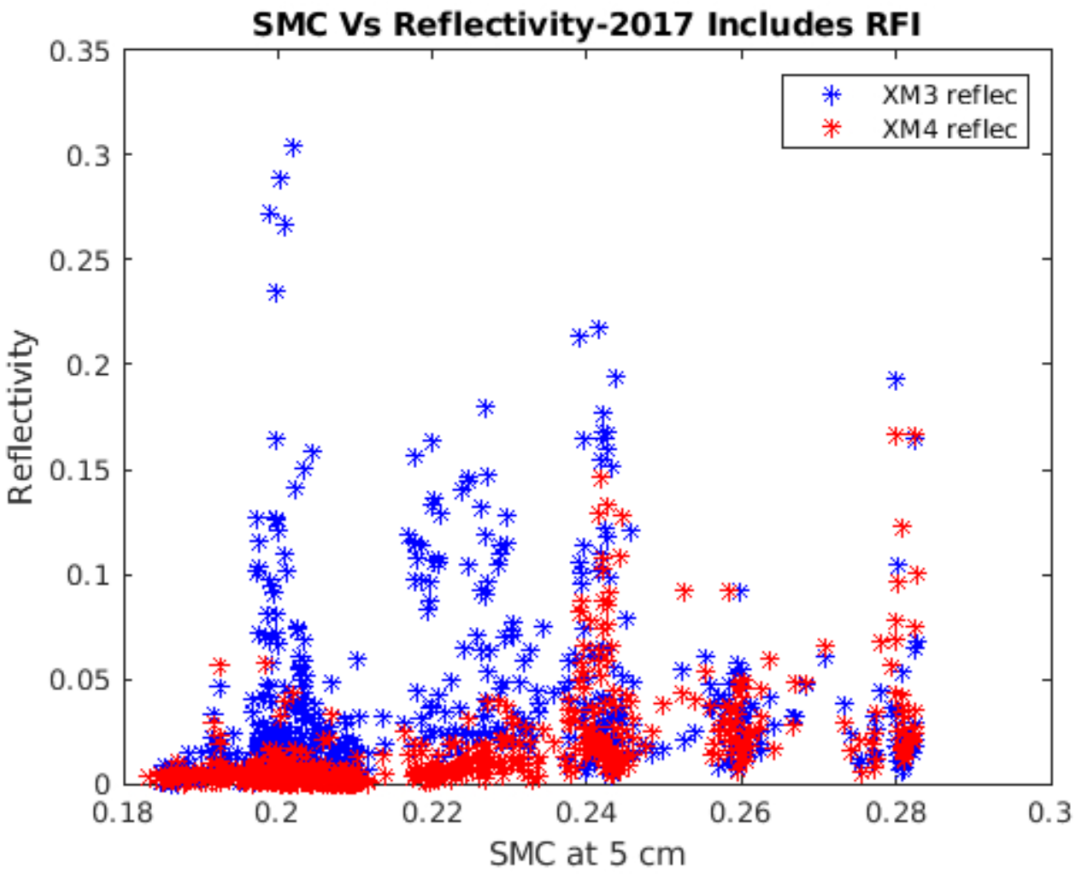

Figure 5.2. Reflectivity VS. SMC at 5 cm. The x-axis represents the SMC values at 5 cm obtained from the Hydraprobes and the y-axis represents the reflectivity retrievals. Both XM-3 and XM-4 frequencies are plotted with respect to the SMC. The legend represents the colour for each XM carrier channel.

moisture across the top of the profile for the 2017 experiment simulator. Each plot uses a different root mean square (RMS) surface roughness measurement for analysis.

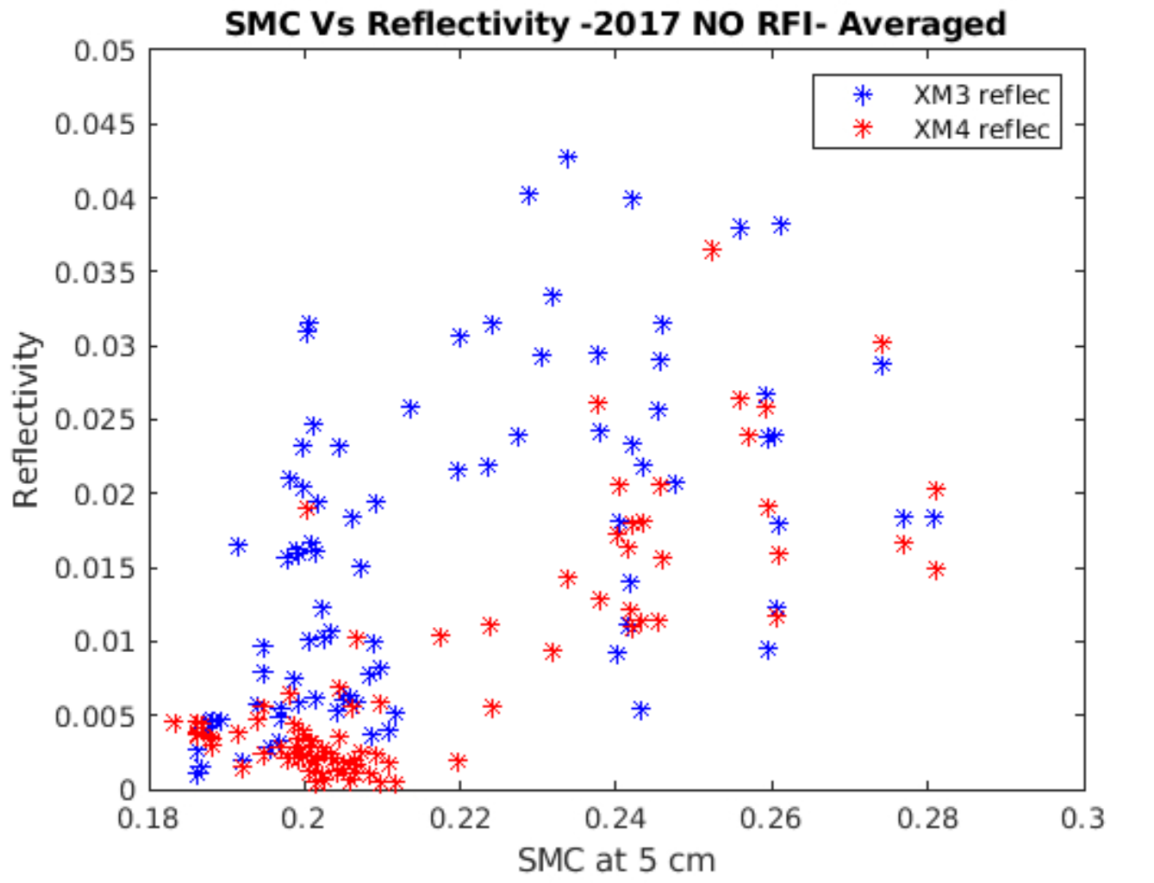

Figure 5.3. Reflectivity VS. SMC at 5 cm. The x-axis represents the SMC values at 5 cm obtained from the Hydraprobes and the y-axis represents the reflectivity retrievals averaged every 1.5 hours and digitally filtered RFI. Both XM-3 and XM-4 frequencies are plotted with respect to the SMC. The legend represents the colour for each XM carrier channel.

Assumption for the simulation

- The surface roughness values are assumed to be 1 cm, 2cm, 2.4 cm, 2.7 cm, 3 cm, and 5 cm for the model. The full soil moisture profile is simulated, albeit the penetration depth for S-band can be 5 cm or less.

- Unaccounted noise in the receiver. Changing of the receiver temperature, unaccounted soil moisture changes, and power from the incoherently scattered radiations are not accounted for in this model.

- Single slab soil moisture fit model assumes for penetration depth as inversely proportional to the attenuation constant. However, ideally, the formulation assumes a flat surface, normal incidence, and complex-valued dielectric constant.

Working of SCoBi model

The ScoBi model converts the SMC values to dielectric constants. The dielectrics are fit into a certain type of fitting model, as listed below, to oil moisture profile points. The fitting functions utilized by [38] are:

- Second order polynomial (2o)

- Third order polynomial (3o)

- Logistic fit

- Slab fit

For the 2017 data, the third-order fit is a cubic function due to which the profile changes drastically (thereby, resulting in high/low near the surface), Second-order polynomial (2o), Logistic fit (ls), and Slab fit (ds, for dielectric slab) fitting functions are used.

The results from SCoBi model for the reflectivity Vs. SMC comparison[1] represented in Fig. 5.4, 5.5, and 5.6. The RMS surface height, s is the surface roughness assumption.

It is observed that as the surface roughness value increases, all the fitting curves in the SCoBi model flatten irrespective of the soil moisture content or reflectivities.

[1]Results for S-band 2017 reflectivity data using SCoBi simulations provided by Dylan Boyd et. al from IMPRESS Lab, Mississippi State University

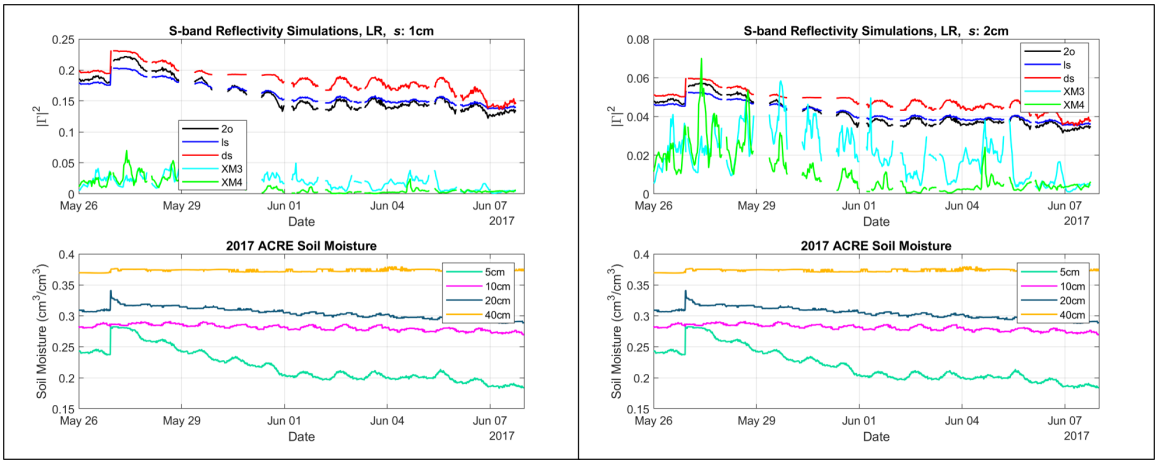

Figure 5.4. SCoBi model simulation Vs reflectivity with respect to time. The surface roughness is assumed to be 1 cm and 2 cm.

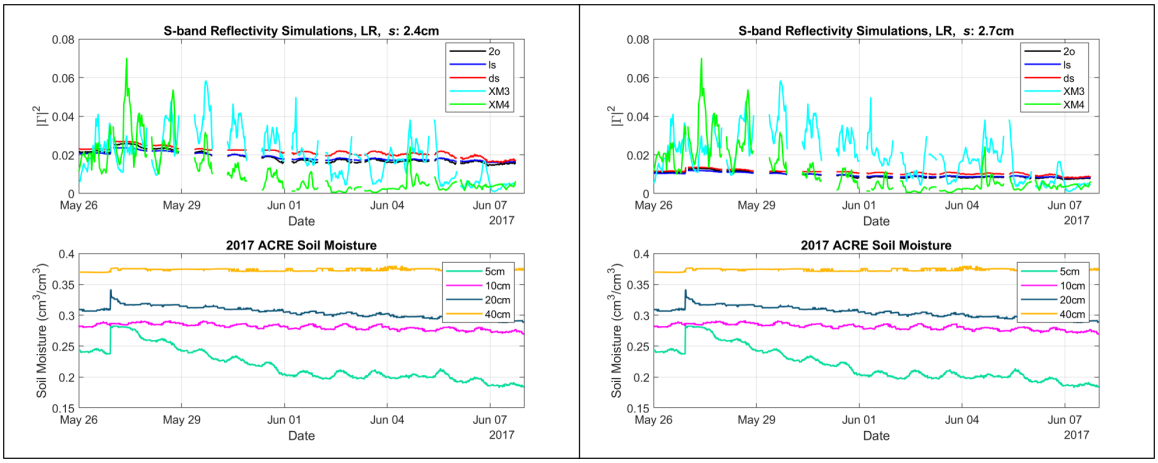

Figure 5.5. SCoBi model simulation Vs reflectivity with respect to time. The surface roughness is assumed to be 2.4 cm and 2.7 cm.

5.2 2018 Preliminary Results

The 2018 S-band tower-based experiment employed two different sky-view and earth-view antennas. They were left hand circularly polarized and right hand cir-

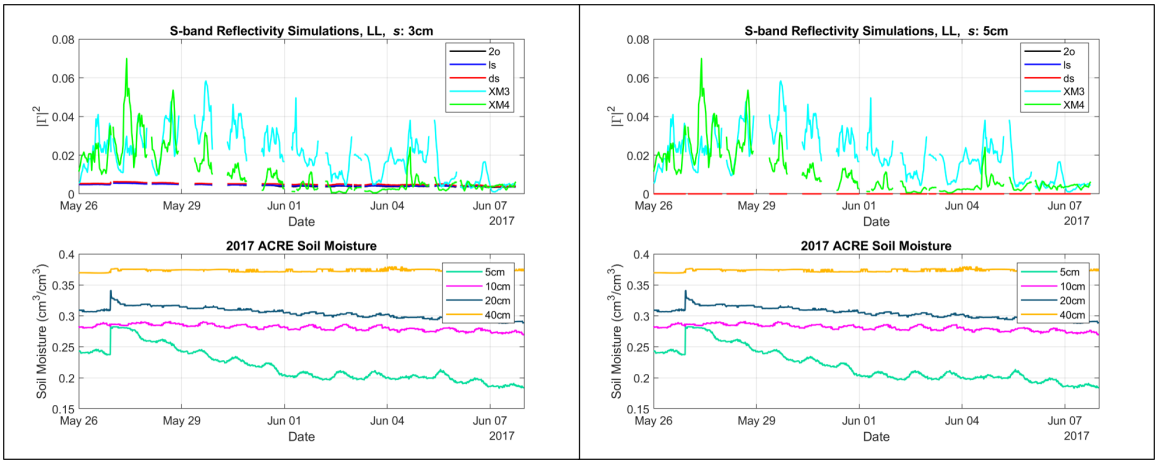

Figure 5.6. SCoBi model simulation Vs reflectivity with respect to time. The surface roughness is assumed to be 3 cm and 5 cm.

cularly polarized (LHCP and RHCP, respectively). Therefore, the reflectivity values were retrieved for XM-3 and XM-4 frequencies, both LHCP and RHCP.

The data was saved separately for XM-3 RHCP and LHCP, and XM-4 RHCP and LHCP .mat files. Reflectivity values LHCP VS. SMC at 5 cm is plotted with respect to time in Fig. 5.7. Similarly, reflectivity values RHCP VS. SMC at 5 cm is plotted with respect to time in Fig. 5.8. The missing data in the plots refers to data being unavailable or corrupt file.

It is noted that the RFI effects mentioned in chapter 4 are present in the 2018 experiments as well, occurring mostly at night from 00:00 to 10:00. This results in an abrupt increase in autocorrelation and cross-correlation values of the channels, and the noise-bands alike. Therefore, the reflectivities abruptly increase which does not depend on soil moisture content. The spikes in reflectivity for the 2018 data could be due to the RFI effects.

The reflectivity VS. SMC for LHCP and RHCP results are plotted separately and compared for XM-3 and XM-4 frequencies. The reflectivity values are averaged every 1 hour, to smoothen the curve and highlight the trend for higher the SMC, higher

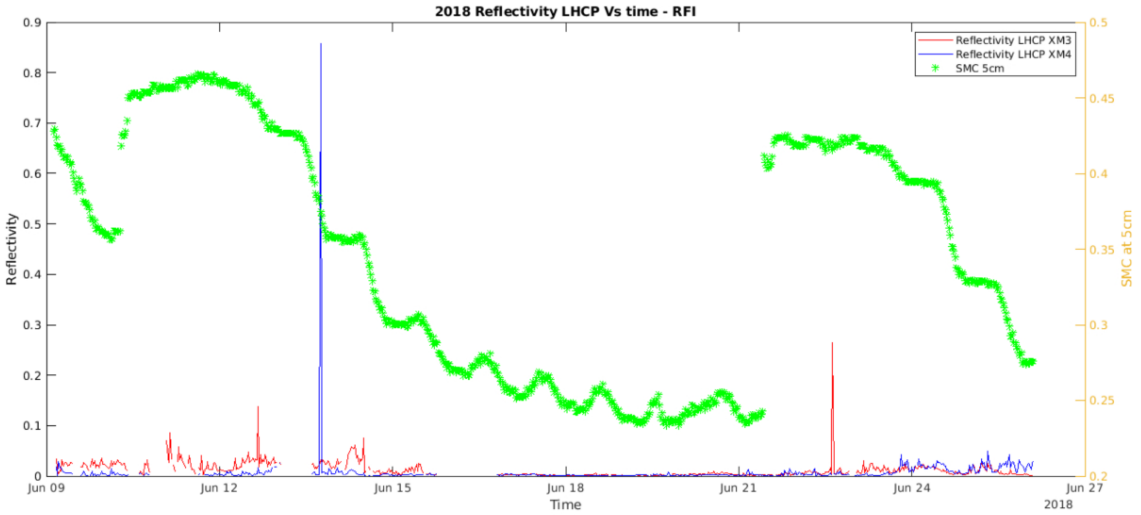

Figure 5.7. Preliminary results for the reflectivity values for received LHCP signals VS. SMC obtained from the HydraProbes at 5 cm depth. The right-hand side y-axis represents the volumetric soil moisture content in percentage. The left-hand side y-axis represents the reflectivity retrieval from the experiment. The x-axis represents the duration of the experiment conducted from 06/09/2018,02:45 to 06/26/2018, 02:15.

the reflectivity values. The SMC VS. reflectivities for LHCP and RHCP are plotted in Fig. 5.9 and 5.10, respectively.

The conclusions inferred are presented in the next chapter along with suggestions for improvement in the future works.

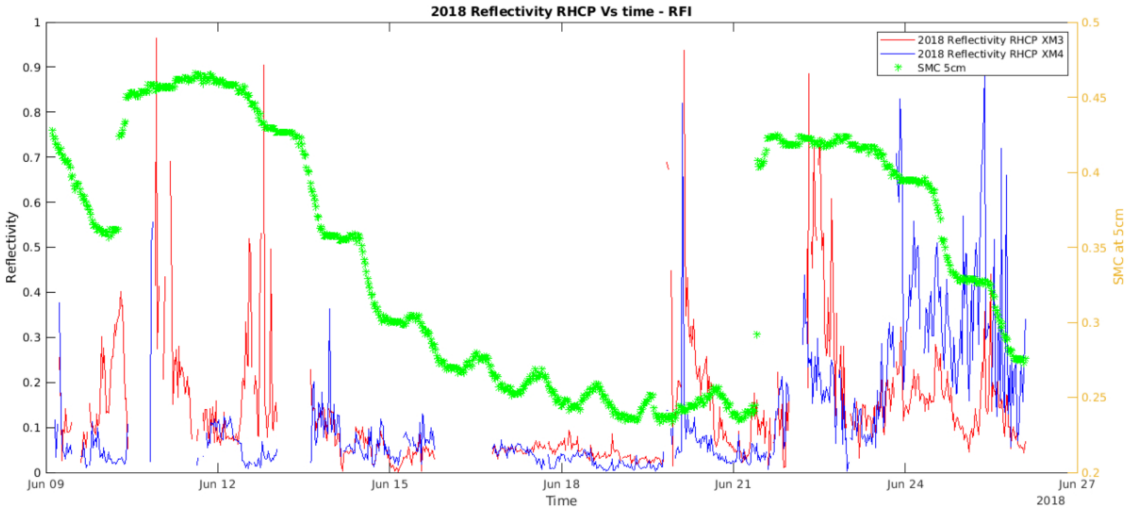

Figure 5.8. Preliminary results for the reflectivity values for received RHCP signals VS. SMC obtained from the HydraProbes at 5 cm depth. The right-hand side y-axis represents the volumetric soil moisture content in percentage. The left-hand side y-axis represents the reflectivity retrieval from the experiment. The x-axis represents the duration of the experiment conducted from 06/09/2018,02:30 to 06/26/2018, 02:30.

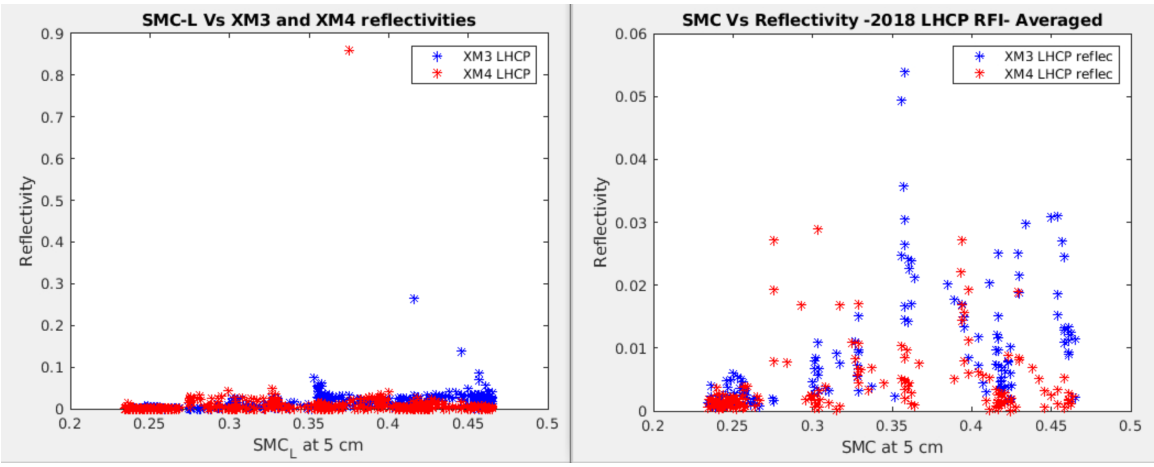

Figure 5.9. Preliminary results for SMC VS. reflectivity values for LHCP XM-3 and XM-4 frequencies. The left-hand side subplot is all the reflectivities for XM-3 and XM-4. The plot on the right is averaged reflectivity for every hour.

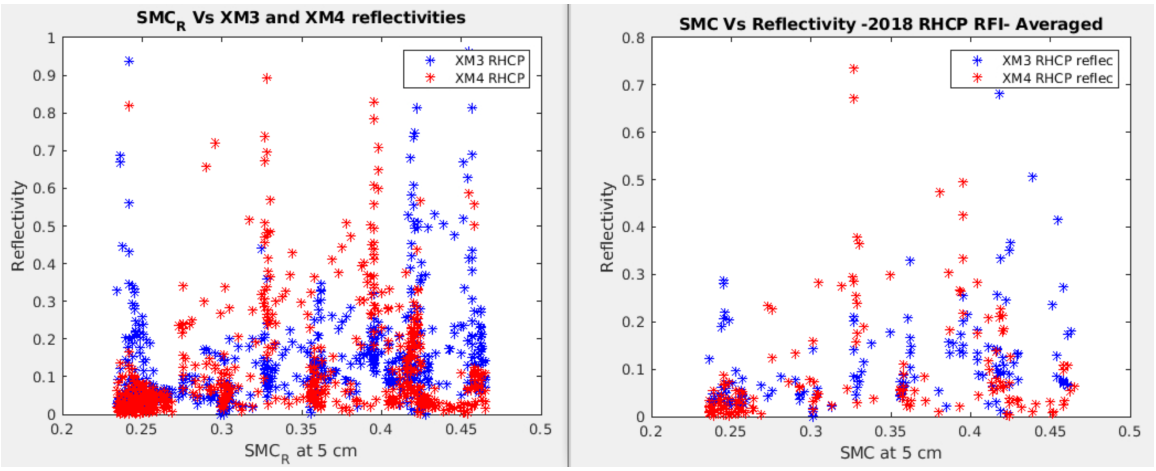

Figure 5.10. Preliminary results for SMC VS. reflectivity values for RHCP XM-3 and XM-4 frequencies. The left-hand side subplot is all the reflectivities for XM-3 and XM-4. The plot on the right is averaged reflectivity for every hour.

6. CONCLUSIONS

In this thesis, data processing was performed for the SoOp tower-based experiments designed and conducted by [10] for the 2017 and 2018 data campaigns. The instrument used S-band and P-band signals for the measurement of soil moisture and above-ground biomass. The instrument was mounted on top of a 32 m tall mobile tower at ACRE, Purdue University. Certain changes were made in the location of sensors, usage of antennas, location of the trailer from 2017 to 2018 data recording.

For the 2017 data, only an RHCP antenna was used to capture the earth-reflected signals. The assumptions for the experiment included specular reflection, perfect isolation of sky-view and earth-view antennas, and coherent reflection. There was also a high amount of RFI recorded in the signals. The RFI and multi-peaks were digitally filtered to provide a result for reflectivity values which likely depend only on SMC. However, the results do show the effects of RFI and incoherence. From the Rayleigh roughness criterion, the incoherent scattering of the reflected signals cannot be assumed to be negligible. However, there is a general trend of reflectivity and soil moisture content for the 2017 data after digitally filtering out the RFI effects and multi-peaks.

For the 2018 data, both LHCP and RHCP earth-view antennas were used to capture reflected signals. XM downlink signals are LHCP. Therefore, after reflection, the signals can be both LHCP and RHCP. As in the case of 2017, there were cases of RFI and multi-peaks in the 2018 data as well. Preliminary results for the 2018 experiment with the effects of RFI in reflectivity retrievals show up as extremely high values abruptly resulting in spikes in the data. However, when the reflectivity results were averaged, the cluster of low reflectivity values at lower SMC values and the almost-linear increase in the reflectivity values as SMC values increased, proving the theoretical basis.

The soil moisture variation near the surface also greatly affects the reflectivity. The 5 cm was a standard for measuring the in-situ soil moisture, however, the evapotranspiration processes occurring in the top layer of soil can affect the reflectivity values.

The SCoBi model utilized full soil moisture profile and each of fitting tool used for the 2017 reflectivity verification, represents a different soil moisture profile. The discrepancies in the reflectivity retrievals from the experiment and the SCoBi model derived from the in-situ data could be due to the surface roughness assumptions, multi-path scattering, and incoherency effects, and unaccounted receiver noise for SCoBi model.

6.1 Suggestions for future work

- The isolation in the earth-view and sky-view antennas can be modeled to be dependent on the antenna gain pattern.
- Multi-path ray model can be used to determine the incoherent backscattering from earth reflected signals.
- For RFI detection and filtering, kurtosis methods can be applied for thorough understanding. [39]

REFERENCES

[1] O. P. N. Calla, D. Bohra, R. Vyas, B. S. Purohit, R. Prasher, A. Loomba, and N. Kumar. *Measurement of soil moisture using microwave radiometer.* 2008 International Conference on Recent Advances in Microwave Theory and Applications, 621-624, 2008.

[2] J. Calvet, J. Noilhan, and P. Bessemoulin. *Retrieving the Root-Zone Soil Moisture from Surface Soil Moisture or Temperature Estimates: A Feasibility Study Based on Field Measurements.* J. Appl. Meteor., 37, 371–386, 1998.

[3] M. Tuller, E. Babaeian, S. B. Jones, C. Montzka, H. Vereecken, and M. Sadeghi. *The paramount societal impact of soil moisture.* Eos,100, 2019.

[4] NOAA. *The Water Cycle.* https://www.noaa.gov/.

[5] T. Delworth and S. Manabe. *The Influence of Soil Wetness on Near-Surface Atmospheric Variability.* J. Climate,1447-1462, 1989.

[6] R.A. Pielke Sr. *Influence of the spatial distribution of vegetation and soils on the prediction of cumulus convective rainfall.* Review of Geophyics, 39(2) 151-177, 2001.

[7] V.Lakshmi. *Remote Sensing of Soil Moisture.* Hindawi Publishing Corporation,ISRN Soil Science, Article ID 424178, 33 pages, 2013.

[8] A.I. Johnson. *Methods of Measuring Soil Moisture in the Field.* United States Government Printing Office, WASHINGTON:1962, 1962. https://pubs.usgs.gov/wsp/1619u/report.pdf.

[9] J. P. Hollinger, J. L. Pierce, , and G. A. Poe. *SSM/I instrument evaluation.* IEEE Transactions on Geoscience and Remote Sensing, vol. 28, no. 5, pp. 781–790, 1990.

[10] B. Nold. *Design of an Instrument for Soil Moisture and Above Ground Biomass Remote Sensing using Signals of Opportunity.* MS thesis, Purdue University, 2019.

[11] *Microwave Remote Sensing.* 2015. https://www.nrcan.gc.ca/maps-tools-publications/satellite-imagery-air-photos/remote-sensing-tutorials/microwave-remote-sensing/9371.

[12] F. T. Ulaby, D. Long, W. Blackwell, C. Elachi, A. Fung, R. Christopher, K. Sarabandi, J. Zyl, and H. Zebker. *Microwave Radar and Radiometric Remote Sensing.* University of Michigan Press, 01 2014.

[13] D. Entekhabi, S. Yueh, P. E. O'Neil, K. H. Kellogg, A. Allen, and R. Bindlish. *SMAP Handbook.* National Aeronautics Administration and Space,Mapping Soil Moisture and Freeze/Thaw from Space, p. 192, 2014.

[14] Y. H Kerr, P. Waldteufel, J.-P. Wigneron, S. Delwart, F. Cabot, J. Boutin, M.-J. Escorihuela, J. Font, N. Reul, C. Gruhier, S. E. Juglea, M.R. Drinkwater, A. Hahne, M. Martin-Neira, and S. Mecklenburg. *The SMOS Mission: New Tool for Monitoring Key Elements of the Global Water Cycle.* Proceedings of the IEEE, vol. 98, no. 5, pp. 666–687, 2010.

[15] *SMAP.* 2015. https://smap.jpl.nasa.gov/observatory/specifications/.

[16] R. Shah. *Analysis Of The Correlation Properties of Digital Satellite Signals and their applicability in bistatic remote sensing.* MS thesis, Purdue University, 2010.

[17] R. Shah, J. L. Garrison, , and M. S. Grant. *Demonstration of bistatic radar for ocean remote sensing using communication satellite signals.* IEEE Geoscience and Remote Sensing Letters, 2012.

[18] J. L. Garrison, Y.-C. Lin B. Nold and, G. Pignotti, J. R. Piepmeier, M. Vega, M. Fritts, C. DuToit, and J. Knuble. *Recent results on soil moisture remote sensing using P-band signals of opportunity.* 2017 International Conference on Electromagnetics in Advanced Applications (ICEAA),pp. 1604–1607, 2017. http://ieeexplore.ieee.org/document/8065595/.

[19] D. Masters, P. Axelrad, and S. Katzberg. *Initial results of land-reflected GPS bistatic radar measurements in SMEX02.* Remote Sensing of Environment, 2004.

[20] K. M. Larson and F.G.Nievinski. *GPS snow sensing: Results from the EarthScope Plate Boundary Observatory.* GPS Solutions, vol 17, 2013.

[21] J. L. Garrison, J. R. Piepmeier, and R. Shah. *Signals of Opportunity: Enabling New Science Outside of Protected Bands.* 2018 International Conference on Electromagnetics in Advanced Applications (ICEAA), Cartagena des Indias,pp. 501-504, 2018.

[22] M. Martin-Neira. *A Passive Reflectrometry and Interferometry Systems.* ESA Journal, 17(4):331–355, 1993.

[23] J.L. Garrison, A. Komjathy, V.U. Zavorotny, and S.J. Katzberg. *Wind speed measurement using forward scattered GPS signals.* IEEE Transactions on Geoscience and Remote Sensing, 40(1):50–65, 2002.

[24] J.L. Garrison, , M.I. Hill, and S.J. Katzberg. *Effect of sea roughness on bistatically scattered range coded signals from the Global Positioning System.* Geophys. Res. Lett, 25(13):2257–2260, 1998.

[25] E. Cardellach and A. Rius. *A new technique to sense non-Gaussian features of the sea surface from L-band bistatic GNSS reflections.* Remote Sensing of Environment, 112(6):2927 – 2937, 2008.

[26] *GPS.* 1978. https://www.gps.gov/.

[27] C. Chew, R. Shah, C. Zuffada, G. Hajj, D. Masters, and A. J. Mannucci. *Demonstrating soil moisture remote sensing with observations from the UK TechDemoSat-1 satellite mission.* Geophys. Res. Lett., 43, 3317– 3324, 2016.

[28] *Cyclone Global Navigation Satellite System (CYGNSS).* 2016. https://www.nasa.gov/cygnss/.

[29] H. Kim and V. Lakshmi. *Use of Cyclone Global Navigation Satellite System (CYGNSS) Observations for Estimation of Soil Moisture*. Geophysical Research Letters, 2018.

[30] M. Cherniakov, D. Nezlin, and K. Kubik. *Air target detection via bistatic radar based on LEOs communication signals*. IEEE Proceedings in Radar, Sonar and Navigation, 149:33–38, 2002.

[31] C. Prati, F. Rocca, D. Giancola, and A.M. Guarnieri. *Passive geosynchronous SAR system reusing backscattered digital audio broadcasting signals*. IEEE Transactions on Geoscience and Remote Sensing, 36(6):1973–1976, 1998.

[32] *WCS and SDARS Spectrum Allocation by FCC*. 2016. https://www.nasa.gov/cygnss/.

[33] *Sirius XM repeaters map*. 2007. http://www.dogstarradio.com/sirius_map.php?state=Indiana.

[34] R. Michalski. *An Overview of the XM Satellite Radio System*. 20th AIAA International Communication Satellite Systems Conference and Exhibit, pp 1844, 2002.

[35] Stevens. *Soil Sensor® Users Manual*. 2018. Tech. Rep.

[36] D. Rowell. *Signal Processing: Continuous and Discrete*. Massachusetts Institute of Technology, Department of Mechanical Engineering - MIT OpenCourseWare, 2008. https://ocw.mit.edu/courses/mechanical-engineering/2-161-signal-processing-continuous-and-discrete-fall-2008/lecture-notes/lecture_22.pdf.

[37] J.McNamee, F. Stenger, and E. L. Whitney. *Whittaker's Cardinal Function in Retrospect*. Math. Comput. 25, 141-154, 1971.

[38] O. Eroglu, D. Boyd, , and M. Kurum. *Open-sourcing of a SoOp simulator with bistatic vegetation scattering model*. Proc. of the IEEE Int. Geoscience and Remote Sensing Symp. (IGARSS), Valencia, Spain, Jul. 23–27, 2018. impress@ece.msstate.edu.

[39] R. D. De Roo, S. Misra, and C. S. Ruf. *Sensitivity of the Kurtosis Statistic as a Detector of Pulsed Sinusoidal RFI*. IEEE Transactions on Geoscience and Remote Sensing, VOL. 45, NO. 7, 2007.

A. TIMELINES OF THE DATA CAMPAIGNS

2017 Field Campaign Timeline		
Date	**Event**	**Notes**
5/23	Campaign Start	
6/09	Pause for corn planting	Tower lowered, front end removed for hardware additions
P-Band horizontal polarization reflected antenna added to tower and front end S-Band RG-8 cables had incorrect connectors, S-Band data was not recorded		
7/08	Microwave recording resumed	Code bug in calibration states, horizontal P-Band state not activated
7/11	Wind storm - tower damaged	Microwave recording stopped, tower lowered
P-Band antenna ground plane mesh changed to chicken wire		
10/10	Recording resumed	Tower was only tilted (10 m high) due to damaged frame
11/04	Campaign end	

Table A.1. 2017 Campaign Timeline [10]

2018 Field Campaign Timeline		
Date	**Event**	**Notes**
5/29	Campaign start	
5/30	P-Band amplifier failed	ZX60-P103LN+ failed, unknown reason
6/23	Began noise recording	
Removed ZX60-P103LN+ only from P-Band amplifier chain, P-Band front end returned to 2017 configuration		
6/27	P-Band front end repaired	
7/09	Temperature sensors stopped recording	Unknown reason
8/11	Last NVDI Measurement	
9/01	Temperature sensors recording resumed	Raspberry Pi restart
10/21	Severe winds, tower damaged	
10/27	Campaign ends	

Table A.2. 2018 Campaign Timeline [10]

Date	**Time**	**Notes**
06/09	11:45 to 14:15	Data Unavailable
06/10	10:30 to 13:00	Data Unavailable
06/11	10:30	Corrupted file
06/13	1:45	Corrupted file
06/13	02:00 to 14:15	Data Unavailable
06/14	15:30	Corrupted file
06/15	19:00 to 23:45	Data Unavailable
06/16	00:00 to 19:00	Data Unavailable
06/17	17:45	Corrupted file
06/18	02:15, 18:30	Corrupted files
06/19	01:15	Corrupted file
06/23	19:45	Data Unavailable
06/26	02:30	Load state stopped working, separate noise files added

Table A.3. 2018 Data Unavailable or Corrupt due to dead battery

B. DATA PROCESSING SCRIPTS

The algorithm used for setting up the location of the files, the data processing for the 2017 and 2018 raw data and the reflectivity retrievals is mentioned below. The scripts are presented in the order of usage. Mostly all the scripts are written to process the 2017 and 2018 data in the same way, except for the data format cases. All the scripts are automated to process any number of files and save all the plots and results in the mentioned folders.

rundatafileprocessing.m

This script is used to setup the location of raw data and the location of results after processing in a .mat format.

Setup script

XMsetup for XM frequencies and MUOS for P-band frequencies. If setup is given as XM-17, then the month-tags and day-tags are set for 05/26/2017 - 06/07/2017. If setup is given as XM-18, then the month-tags and day-tags are set for 06/09/2018 - 06/26/2018

The files are searched from the function 'filedatabase.m' The path to results is set. Pre-allocation for the resultant .mat file with the variable as columns and number of files as rows

filedatabase.m

This function in set up as a way of inputting the file names and locations for each day. Generally organized to allow processing of one day blocks at a time - Structure member are: prefix = path prefix of the directory to the files (generated with a master prefix) fname-mat = string array of file names for each day - existence verified.

First group of observations - correspond to the bare-soil measurements made at ACRE May 25-June 8, 2017

function dayfilestruct = filedatabase(setup)

Returns the number of valid files found in the database for the given setup.

quickLook.m

The files are setup according to the command in setup command. The sampling frequency, window length, number of iteration, etc are set here.

The files from the file database are open here for reading in text format and identifying the bit from where the actual data starts.

Pre-allocation of variable in gpuArrays for faster and efficient calculations and storage.

For the channel of interest (XM-3 or XM-4), the lower noise band and the higher noise band, the autocorrelation of direct, reflected and the cross correlations are calculated for the number of iterations

This script reqiures XMsetup.m, stateparser.m, correlationPlotter.m, plotSingle-Datawindow.m, specularpointtracking.m to run as desired.

XMsetup.m The XM-17 and XM-18 setups are unified in this code. All the required variables such as sampling frequency, window length, number of integration, integration time, filter setup are included in this script.

Stateparser.m

This script parses the calibration states for XM-17, XM-18, MUOS-17 and MUOS-18 depending on the information given in the setup file. This script requires state verification script for producing state parsed plots. This is a unified code with specific parts initialized by conditions according to the setup.

Correlationplotter.m requires timetag -¿ time in sec for X-axis requires correlation values for direct,reflect,cross_channel, noise_high(direct/reflect/cross) and noise_low(direct/refle

This script plots autocorrelations and cross-correlations for the channel, lower-end and higher-end noise bands

This script also plots the phase correlations for 2017 and 2018

plotSingledataWindow.m

This script is used in quickLook.m for plotting PSD of the direct signal (filtered and unfiltered), reflected signal (filtered and unfiltered). Also plots the magnitude of autocorrelation and cross-correlations for both XM and MUOS data (2017 and 2018).

SpecularPointTracking.m Used for specualr point tracking as mentioned 4.2.2

reflectivity-calc.m

This script is separately written to read the .mat files of autocorrelations and cross-correlations for the 2017 and 2018 data. This script uses equation 3.49 for reflectivity retrievals and plotting them against time or SMC at 5 cm from the HydraProbes data at half-tile configuration.